Floating hollow carbon spheres for improved solar evaporation

A. Celzard, Andreea Pasc, S. Schaefer, K. Mandel, T. Ballweg, S. Li, G. Medjahdi, V. Nicolas, Vanessa Fierro

Floating hollow carbon spheres for improved solar evaporation

A. Celzard[1*], A. Pasc[2], S. Schaefer[1], K. Mandel[3,4], T. Ballweg[3], S. Li[2], G. Medjahdi[5], V. Nicolas[1] and V. Fierro[1]

[1] Université de Lorraine, CNRS, IJL, F-88000 Epinal, France

[2] Université de Lorraine, CNRS, L2CM, F-54000 Nancy, France

[3] Fraunhofer Institute for Silicate Research ISC, D-97082 Würzburg, Germany

[4] Chair of Chemical Technology of Materials Synthesis, Department Chemistry and Pharmacy, Julius-Maximilians-Universität Würzburg Röntgenring 11, 97070 Würzburg, Germany

[5] Université de Lorraine, CNRS, IJL, F-54000 Nancy, France

[*] Corresponding author. Tel: + 33 372 74 96 14. Fax: + 33 372 74 96 38. E-mail address : alain.celzard@univ-lorraine.fr (A. Celzard)

Abstract

Hollow carbon spheres (HCSs) were prepared from sugar alcohols encapsulated in UV-cured polymer which were hydrothermally treated in solutions of carbon precursors and carbonised at different temperatures in the presence or absence of graphitisation catalysts (Fe(III) and Ni(II)). The resultant HCSs were then spread at the surface of salt water and submitted to a solar simulator in a special ventilated chamber. The presence of HCSs floating at the surface of water was shown to increase significantly the evaporation rate compared to an HCS-free reference. The effect of carbon precursor, pyrolysis temperature, size and presence of metal was investigated and discussed. The best performances were obtained with nickel-loaded HCSs treated at 1500°C, leading to a water evaporation rate increased by 70% with respect to the reference. These performances were discussed in terms of floatability, the latter being related to wettability, composition and apparent density of the HCSs. A model was developed for separating the contributions of floatability and thermal conductivity, definitely demonstrating that the former was the key parameter explaining the performances of floating HCSs for evaporating water submitted to a radiant heat flow.

Keywords: Template method; Hydrothermal carbonisation; Hollow carbon spheres; Graphitisation; Solar evaporation; Modelling

1. Introduction

Hollow carbon spheres (HCSs) are a new class of carbon materials for which the researchers' interest is growing rapidly worldwide [1]. The name they were given unambiguously refers to very lightweight spherical particles, whose diameter can range from nanometre- to millimetre-size, and basically consisting of one single thin outer shell and a hollow core, although multi-shelled HCSs have also been reported [2,3]. The shell can be more or less porous and bear some functional groups. As a result, some HCSs can develop high surface area and, depending on the pore size and thanks to the presence of a central cavity, they have been suggested for a number of applications, ranging from environment (treatment of water [4,5] or entrapment of toxic gases [6,7]), catalysis of various reactions [8,9], energy (electrode material for fuel cells [10-12], batteries [13-15] or supercapacitors [16–23]), amongst others (picolitre containers [24,25], hydrogen storage materials [26,27], basic units for electromagnetic metamaterials [28,29], sacrificial templates [30,31], etc.). All these applications as well as the corresponding synthesis processes have been reviewed in a recent paper [1]. In parallel, and not cited in the latter review, biomedical applications were also suggested, such as drug delivery [32,33], immobilisation of enzymes [34,35] and bioimaging [36,37].

Recently, a new application emerged: concentrating solar heat for boosting the evaporation of water [4], and thus producing pure water or steam from seawater for instance. Currently, steam generation using solar energy is indeed based on heating bulk water above its boiling point. This approach requires either expensive high light intensity leading to heat loss by the hot bulk liquid and heated surfaces, or vacuum [38]. New solar receiver concepts such as porous volumetric receivers [4,38] or nanofluids [39,40] have been proposed to decrease these losses. Efficient harvesting of solar energy for steam generation is a key factor for a broad range of applications,

from large-scale power generation, absorption chillers and desalination systems to compact applications such as water purification for drinking, salt-making industry, and sterilisation and hygiene systems in remote areas where the only abundant energy source is the sun. A solar evaporation process with higher efficiency would thus be very welcome [41].

Carbon is known as an excellent photothermal material with high absorbance and low emittance [42]. Owing to their lightness, HCSs arranged in a monolayer are expected to float on the surface of the water where evaporation occurs, and should therefore minimise heat losses and result in improved solar evaporation. Since the issue of solar evaporation is of great significance, the potential of polymer capsules-templated HCSs as solar steam generation enhancers that do not require vacuum is worth investigating. Combining the well-known chemical inertness of carbon at moderate temperature and its light-absorption properties, floating HCSs might indeed absorb sunlight and then convert it to thermal energy, resulting in an increase of the surface temperature of water and a significant enhancement of the water evaporation rate.

The present study thus aimed at observing such an effect, using HCSs prepared from sugar alcohols encapsulated in UV-curable polymer shells, then submitted to hydrothermal carbonisation in the presence of a carbon precursor, with or without metal salts, and finally pyrolysed. The paper is organised as follows: first, the preparation of HCSs is detailed, with some focus on the way the carbon nanotexture of the final materials can be modified by changing their synthesis parameters. Then, the characterisation methods and the experimental set-up for mimicking solar evaporation are described. The evaporation rates of water covered by a monolayer of different kinds of HCSs and submitted to a solar simulator are then discussed, with emphasis on the effect of various parameters on the evaporation rate: HCS size, nature of carbon precursor, temperature of pyrolysis, and presence of metal in the carbon shell. Finally, we show

that modelling the evaporation process allows understanding the reason why some HCSs are better than others for this application: their floatability, complex combination of density and wettability, and not their thermal conductivity.

2. Experimental

2.1. Materials

The general protocol used herein for producing HCSs is given in Fig. 1, and is known as hard-templating [1]. It requires first the preparation of spherical templates of well-defined diameters, and then the conversion of these templates into HCSs according to two successive steps: (i) coating of the spheres with a carbon precursor; and (ii) pyrolysis of the resultant material. In the latter step, the coating transforms into a hard carbon shell, whereas the core of the spherical template condenses on the inner surface of the shell and gives an additional amount of carbon. As a result, a hollow carbon sphere is obtained.

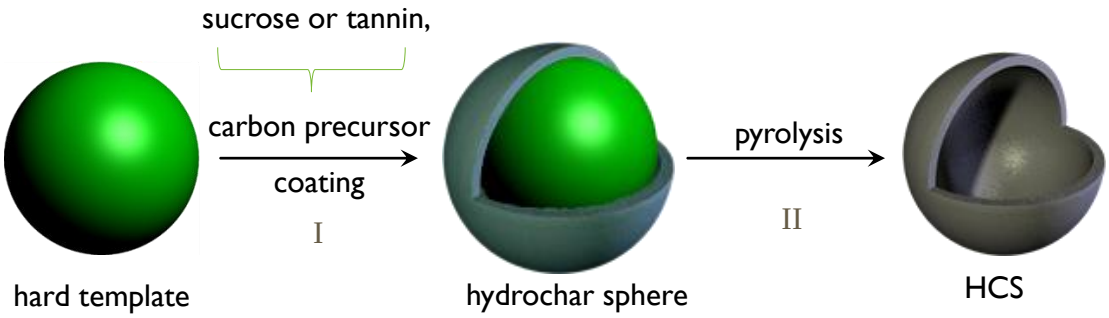

Fig. 1. General scheme of the hard-templating method for preparing hollow carbon spheres (HCSs).

2.1.1. Preparation of spherical templates

Herein, polymer spheres prepared by encapsulation of xylitol-erythritol (64:36 in mol. %) in UV-curable resin were used as templates for the preparation of HCSs. Such materials were

initially developed for seasonal thermal storage (the melting point of xylitol-erythritol eutectics is 82°C, with an enthalpy as high as 278.7 J g^{-1}) [43], and were advantageously used here because they contain sugar alcohols. The shell of such capsules is indeed too thin and with a too low carbon yield for surviving any direct pyrolysis process. However, even while filled with sugar alcohols (empty spheres behave even worse), these polymer beads had to undergo a hydrothermal carbonisation (HTC) process in the presence of an additional carbon precursor: sucrose or tannin dissolved in water. Nevertheless, due to the perfect control over size and sphericity allowed by the method described below for preparing the polymer spheres, this template intermediate was of high value to obtain HCSs by HTC.

Xylitol-erythritol – filled polymer shells were obtained by using the special device which was recently described in detail elsewhere [44]. In brief, the basic apparatus consists of two pressurised steel-recipients for core and shell materials, which are then fed through an annular nozzle-system mounted on a tuneable oscillator. The core material (xylitol-erythritol blend) and the shell material (ethoxylated triacrylate (TMPTAE) with 6 PEG segments per unit) are extruded simultaneously through the nozzle system, with the core material in the centre and the shell material in the outer ring. With the nozzle head placed on a vibrator, a transversal vibration is superimposed to the stream which generates equidistant constrictions leading to droplet separation [44]. The droplets subsequently pass by a high-power UV radiator with ellipsoidal reflector while falling towards the ground which ultimately causes UV-induced crosslinking of the shell material.

By changing the nozzle diameter, the exit velocity of the stream, and/or the operating frequency, 30 to 2000 droplets per second, having uniform and adjustable size, can be obtained. As the encapsulation process is very fast, less than one tenth of second, the capsules can be

collected immediately after leaving the curing zone. The set-up is shown in Fig. 2, with which two sizes of spheres were obtained: “big” (~ 2.6 mm in diameter) and “small” (~ 1.8 mm).

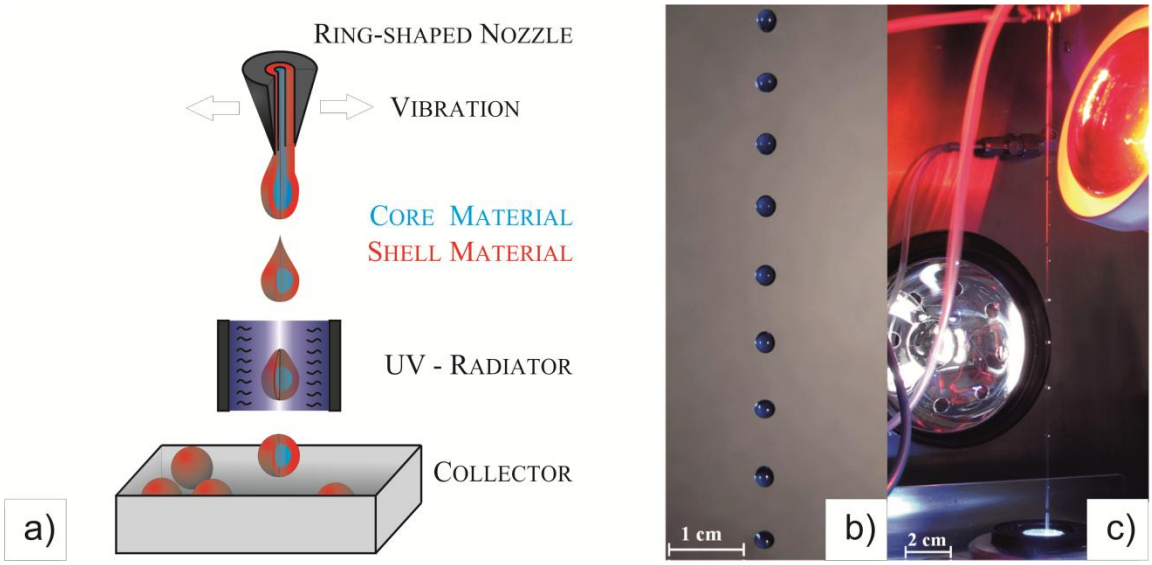

Fig. 2. “(a) Scheme of the preparation of UV-cured polymer capsules containing sugar alcohols; (b) photo of the as-obtained drop falling from the vibrating nozzle captured with a high-speed camera; (c) same as (b) but observed with a stroboscope before the drop enters the UV-curing zone through an iris diaphragm” (reprinted from [44] with permission from Elsevier).

2.1.2. Conversion into HCSs

After the spherical polymer capsules were recovered, various kinds of hydrothermal treatments were applied. All consisted in putting 2 g of spheres (i.e., a few tens, depending on their size) in a glass vial placed in a 38 mL Teflon-lined, stainless steel autoclave. The inner volume of the autoclave was then filled at one third of its capacity with an aqueous solution of two possible carbon precursors shown in Table SI1 of the Supplementary Information. Sucrose and mimosa tannin are both relevant natural precursors producing a high yield of hydrothermal carbon, as shown by many former works on this topic, for instance [45-49]. The hydrothermal carbonisation

(HTC) was then carried out by placing the autoclave in a pre-heated oven at 180°C for 24 h. After that, the materials were naturally cooled down to room temperature before opening the autoclave.

Depending on the nature of the precursors, the shells of the resultant HCSs were expected to have different final carbon textures. The nanotexture, checked by Raman spectroscopy (see below), was modified further by adding metal salts to sucrose solutions, especially those known to behave as graphitisation catalysts at high temperature such as iron and nickel [50]. For better observing the effect of metal loading, the highest concentration of metal salts was tested in the autoclave. It was found that a concentration of Fe(III) of 0.1 mol L^{-1} (pH around 1.6) was the highest possible without damaging the resultant carbon spheres, probably because of the very acidic conditions. As for Ni(II), concentrations as high as 5 mol L^{-1} were possible, but the major part of the nickel precipitated apart in the form of hydrated oxide. A concentration of 1 mol L^{-1} was then chosen instead, for which such phenomenon was quite limited, the major part of the nickel depositing inside the carbon shell.

Finally, the spherical hydrochars recovered from the autoclave, whether loaded with metal or not, were washed several times with deionised water and dried in air at room temperature. Once perfectly dry, they were pyrolysed in a ceramic boat placed at the middle of a quartz tube flushed with high-purity nitrogen at various temperatures (2°C min^{-1}, 2h dwell time) to produce HCSs. The synthesis conditions, as well as the corresponding sample names, are presented in Table 1.

Table 1. Preparation conditions of HCSs and corresponding sample names, with emphasis on the effect of each parameter**.** "PB" and "PS" stand for polymer beads of bigger (~ 2.6 mm in diameter) and smaller size (~ 1.8 mm), respectively. The letter that follows in the label indicates the carbon precursor: "S" for sucrose, "T" for tannin, "C" for carbonised, and the number stands for the amount (in g) of the carbon precursor. "Fe"- or "Ni"-marked samples are the corresponding counterparts loaded with iron(III) or nickel(II), respectively.

Sample name	Carbon precursors	Solution	Pyrolysis temperature (°C)
Effect of the size of the templates, at two different pyrolysis temperatures			
PBS1.0C-900	1.0 g sucrose	water	900
PSS1.0C-900	1.0 g sucrose	water	900
PBS1.0C-1500	1.0 g sucrose	water	1500
PSS1.0C-1500	1.0 g sucrose	water	1500
Effect of the nature of carbon precursors, at fixed pyrolysis temperature			
PBS1.0C-1500	1.0 g sucrose	water	1500
PBT1.0C-1500	1.0 g tannin	water	1500
Effect of metal loading, at constant size of template, and at two different pyrolysis temperatures			
PBSFeC-900	1 g sucrose	0.1 M $FeCl_3$	900
PBSNiC-900	1 g sucrose	1.0 M $Ni(NO_3)_2$	900
PBSFeC-1500	1 g sucrose	0.1 M $FeCl_3$	1500
PBSNiC-1500	1 g sucrose	1.0 M $Ni(NO_3)_2$	1500

2.2. Characterisation methods

The morphology and the general structure of the materials were mainly characterised by scanning electron microscopy (SEM), using a Hitachi S-4800 Field Emission SEM apparatus. The

samples were fixed on an aluminium support with an adhesive carbon tab and coated with an ultrathin (3–5 nm), sputtered carbon layer. Energy Dispersive X-ray analysis (EDX) was also made for the qualitative chemical investigation of the as-obtained SEM pictures.

Elemental analysis was carried out with a Vario EL cube (Elementar) analyser for determining the oxygen content of the hollow carbon spheres after pyrolysis. For that purpose, samples of a few mg were ground and wrapped in a tin foil, and then submitted to a flash combustion at 1200°C in an excess of gaseous O_2 carried by helium. The combustion products, CO_2 and H_2O, were both reduced on a hot column of charcoal into CO, which was next quantified by a chromatographic system. The oxygen content of the materials was then deduced after calibration with known (organic molecules) standards.

Carbon nanotexture assessment was performed by X-ray diffraction (XRD) and Raman spectroscopy. XRD patterns were recorded with an MPD PANalytical X'Pert Pro diffractometer. The latter was used in a Bragg-Brentano configuration in reflection mode and was equipped with a Cu (K_α radiation) anticathode and a high-speed multichannel X'Celerator detector in scanning mode. Raman spectroscopy was carried out using an XploRa Raman spectrometer (Horiba) without sample preparation. The spectra were collected under a microscope using a 50 × objective. The Raman-scattered light was dispersed by a holographic grating with 1200 lines/mm and detected by a CCD camera. A laser of wavelength 532 nm was used, i.e., corresponding to incident energy of 2.33 eV, filtered at 10% of its nominal power for avoiding any heating or damage of the samples. Each spectrum was obtained by accumulation of 2 spectra recorded from 200 to 3700 cm^{-1} over 120 s. Different areas of each type of HCS were analysed, giving some information about the homogeneity of the materials.

As for mechanical properties, a very rough estimation was made by submitting 3 randomly chosen spheres of PBS1.0C-900 to reference weights until they were irreversibly crushed.

For measuring the water contact angle (WCA) on carbon shells, the method used elsewhere [4] consisting in making a pellet from ground HCSs, was not applicable here because of the brittleness of the constitutive carbon, inducing the impossibility of preparing a self-standing, binderless pellet (using a binder such as polymer would have dramatically affected the wetting properties). At the same time, the very rough and spiky surface of such pellet made of broken carbon shells would have disturbed the measurement and probably led to high WCAs, irrespective of the surface chemistry.

The hydrophilic/hydrophobic character of HCSs was thus evaluated with a Drop Shape Analyser DSA100 (Krüss), by depositing water droplets of less than 0.1 µL at the top of a few HCSs attached to a horizontal support with modelling clay. Despite the diameter of the droplets was much lower than that of the HCSs, using a linear baseline for determining the WCA proved to be poorly accurate, even if some differences between materials could already been clearly evidenced. The WCA was thus corrected from the convexity of the HCS surface, otherwise leading to an overestimation of the contact angle, according to the method described elsewhere [51]. The principles are schematised in Fig. SI1a of the Supplementary Information, and the true WCA, $\theta_{a,0}$ (°), was calculated as:

$$\theta_{a,0}(°) = \theta_a(°) - \frac{180}{\pi} sin^{-1}\left(\frac{a}{R}\right) \quad (1)$$

where θ_a (°) is the apparent contact angle deduced from a horizontal linear baseline, a is the half-length of the chord that subtends the arc defined by the contact between the drop and the HCS surface, and R is the HCS radius.

This way of doing was not free of error due to the uncertainties both on the diameter of the HCS and on the chord length. Therefore, another method was also tested, using a curved baseline that fits the contour of the HCS, see Fig. SI1b. Doing such fit was allowed by the software of the drop shape analyser, and led to values slightly different from those obtained by the aforementioned protocol. Whatever the method, the WCA was recorded as a function of time.

Another property worthy of interest is the floatability of HCSs, which is even more relevant to the present situation: floatability is indeed related both to wettability and to specific weight, the latter two characteristics possibly being antagonistic in some cases. It may be anticipated that a poor wettability combined with a low specific weight leads to a low contact area between HCSs and water, and hence to a poor thermal transfer. On the contrary, a good wettability associated with a high specific weight would make the HCSs sink too deep, therefore leading to a low efficiency in terms of evaporation rate, which is a surface phenomenon. All intermediate situations between the aforementioned extreme ones are possible, and should lead to some compromise.

The height of floating HCSs from the water level was thus measured with a cathetometer, i.e., an instrument for measuring accurately the vertical distance between two points and consisting of a horizontal telescope (with crosshair) capable of being moved up and down a rigid vertical column equipped with a graduated (Vernier) scale. The latter allowed an accuracy of less than 0.05 mm. HCSs from various (but not all) families presented in Table 1 were first dried for 1h in a ventilated oven at 105°C, followed by 30 min at 85°C in a vacuum oven (residual pressure lower than 50 mbar). They were individually weighed with a high-accuracy (0.01 mg) balance, their diameter was measured, and then they were gently placed at the surface of 3.5 wt.% NaCl salt water. Due to the very rough surface of certain HCS families, some kind of Lotus effect was sometimes observed, leading to the metastable position shown in Fig. 3a and called “minimum

wetting". In such a case, the centre of the spheres remained well above the water level, and for some HCSs, such situation lasted quite a long time as far as the system was not disturbed. However, a preliminary wetting of all HCSs led to the situation called "maximum wetting" shown in Fig. 3b, i.e., with the spheres centres below the water level. Such situation was stable for months (see below). Only the latter situation should obviously be considered for a long-term application; however the metastable situation was investigated as well.

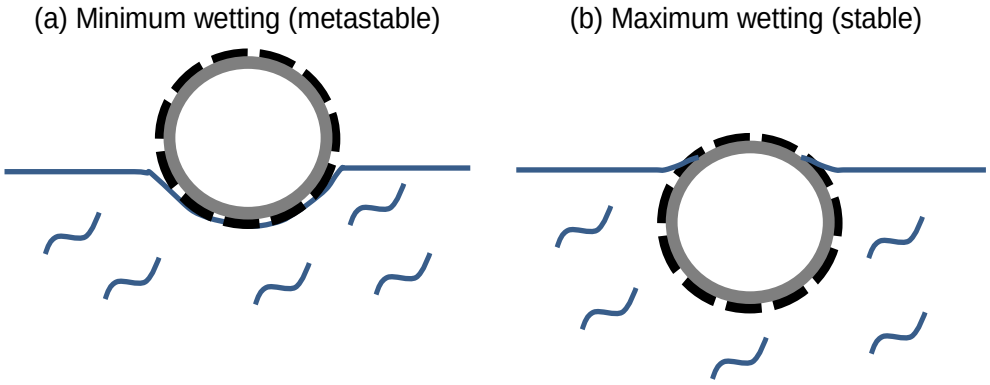

Fig. 3. Two situations after depositing HCSs at the surface of salt water. The thick dashed line around the carbon shell represents the roughness of its surface due to the deposition of hydrochar during the HTC process (see next section).

2.3. Solar evaporation

Water evaporation was performed at room temperature using the lab-made experimental setup shown in Fig. 4. The solar evaporation chamber was ventilated for better controlling the evaporation flow and stabilising the measurements, which had not been done in former works on a similar topic. In other words, we worked in a forced convection mode, not in a natural flow regime. In a typical test, three identical beakers (2.8 cm of inner diameter) were filled with 20 g of 3.5 wt.% NaCl salt water (thus simulating seawater), and installed together in the chamber. An AM 1.5G solar concentrated light simulator (Solaronix, based on a Lumixo light engine) was used

with the three following power densities: 0.8, 1, and 1.3 kW m^{-2}. One beaker was free of HCSs and was used as reference, whereas the water surface of each of the other two beakers was covered with a complete monolayer of HCSs having the characteristics already presented in Table 2. Each measurement was carried out for 3.5h, during which all beakers were carefully weighed every 30 min, and the data from the two beakers covered with HCSs were averaged. From the 8 experimental points thus obtained, i.e., including the one at $t = 0$, straight lines were obtained from which the slope gave the evaporation rate, expressed in kg of water evaporated per m^2 of HCS monolayer and per hour.

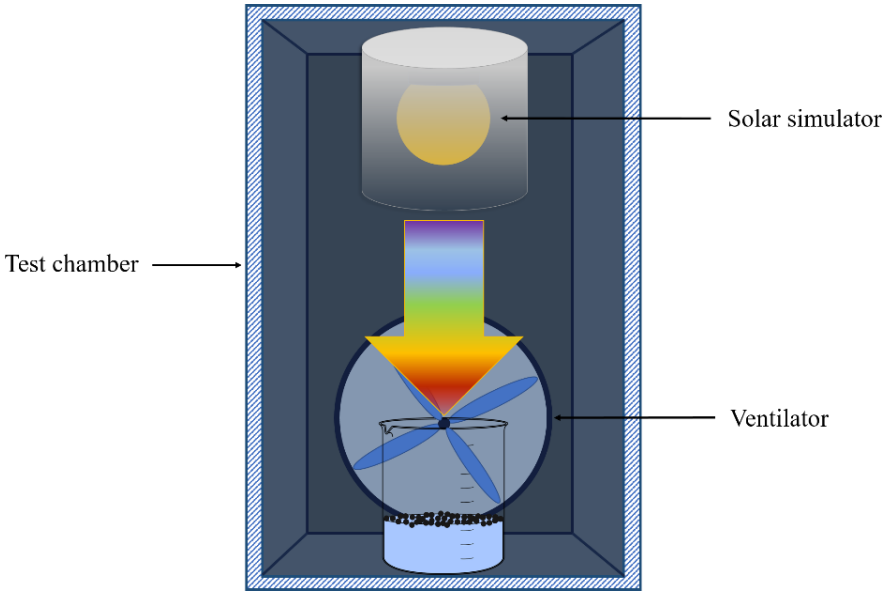

Fig. 4. Experimental setup for solar water evaporation measurements. For clarity, only one beaker is shown instead of three in reality.

2.4. Modelling

The evaporation rate of a simple system of spheres floating at various levels from below to above the water level was modelled by considering the following simplifying assumptions: (i) the radiation absorbed by water is considered as a source term proportional to the incident radiation; (ii) the air temperature is constant; (iii) the water vapour pressure is constant in the chamber, (iv)

the spheres are packed according to a 2D square lattice. The modelling consists first, based on the weight loss measurements as a function of time, in calculating the evaporation flow rate of the HCS-free system, and then in adding the HCSs to the system and in observing the corresponding changes of evaporation rate. The physical model was implemented with Comsol Multiphysics v5.2a commercial software with heat transfer toolbox using the finite element method.

The considered geometry is the one shown in Fig. 5a, where T_a (K) is the temperature of air, h_c (W m^{-2} K^{-1}) is the convective exchange coefficient, and F_m (kg m^{-2} s^{-1}) is the evaporation mass flux. The heat flux is set to zero laterally but non-zero at the top and at the bottom of the system. In these conditions, the heat equation reads:

$$\rho c_p \frac{\partial T}{\partial t} + \vec{\nabla} \cdot \left(-\lambda \vec{\nabla} T \right) = P_{abs} \text{ for the considered domain,} \quad (2)$$

$$-\vec{n} \cdot \left(-\lambda \vec{\nabla} T \right) = h_c \left(T_a - T \right) + F_m L_v \text{ at the upper limit of the domain for air / water interface} \quad (3)$$

$$-\vec{n} \cdot \left(-\lambda \vec{\nabla} T \right) = h_c \left(T_a - T \right) \text{ at the upper limit of the domain for air / HCS interface} \quad (4)$$

$$-\vec{n} \cdot \left(-\lambda \vec{\nabla} T \right) = \frac{\left(T_a - T \right)}{R_c} \text{ at the lower limit of the domain,} \quad (5)$$

$$\text{and } -\vec{n} \cdot \left(-\lambda \vec{\nabla} T \right) = 0 \text{ on the sides of the domain} \quad (6)$$

where ρ, c_p, λ and L_v are the density (kg m^{-3}), the specific heat capacity (J kg^{-1} K^{-1}), the thermal conductivity (W m^{-1} K^{-1}) and the latent heat of evaporation of water (J kg^{-1}), respectively, R_c (m² K W^{-1}) is the thermal contact resistance with the chamber, P_{abs} (W m^{-3}) is the volume power absorbed by water, $\vec{n}$ is the normal vector, and T (K) is the temperature.

Moreover, radiative heat transfer is considered in the physical problem. A radiant flux is simulated above the carbon sphere, which is assumed to be a black-body material. The mathematical problem is directly operated by the heat transfer toolbox of the software.

The evaporation heat flux reads:

$$F_m = -k_m \frac{M_v}{R}\left(\frac{p_{v;a}}{T_a} - \frac{p_v}{T}\right) \quad (7)$$

where M_v (kg mol^{-1}) is the molecular weight of water, R (J mol^{-1} K^{-1}) is the universal gas constant, and $p_{v;a}$ and p_v (Pa) are the water vapour pressure in air and at the water surface, respectively. k_m (m s^{-1}) is the convective mass exchange coefficient, calculated as:

$$k_m = h_c / 1000 \quad (8)$$

following Colburn's analogy. Combining Eqs. (3), (7) and (8), one gets:

$$-\vec{n}\cdot\left(-\lambda\vec{\nabla}T\right) = h_c\left(T_a - T\right) + \left(-\frac{h_c}{1000}\frac{M_v}{R}\left(\frac{p_{v;a}}{T_a} - \frac{p_v}{T}\right)\right)L_v \quad (9)$$

at the upper limit of the domain for air/water interface. Eq. (9) shows that the h_c coefficient is finally the only unknown in a system without radiant heat flux. The experimental data given in the next section will then give access to its value.

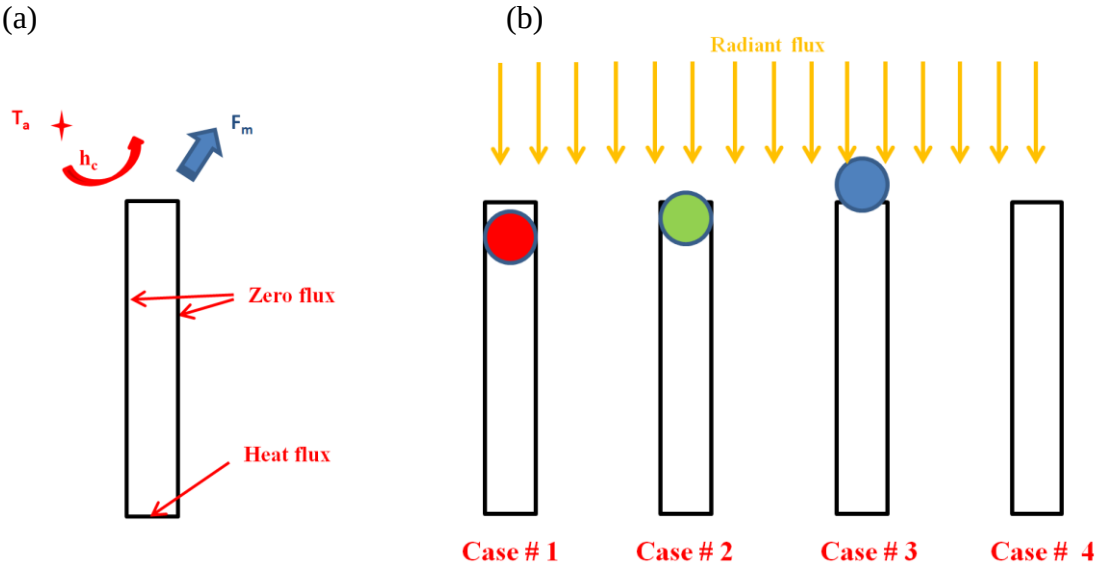

Fig. 5. Simple geometry of a water column of square cross-section submitted to a radiant heat flux from above: (a) without HCS; (b) with one HCS whose diameter is equal to the side of the water column cross-section, and at various heights with respect to water level (the HCS is removed in case #4).

The second step of the modelling thus consists in parametric studies in which 3 cases with HCS and one without HCS are considered, see Fig. 5b. In the 1st case, the HCS is totally immersed, i.e., is far below the water level, the 2nd case considers a floating HCS with less than half its volume emerged, and the 3rd case corresponds to more than half of the HCS volume emerged. Cases #2 and #3 thus correspond to Fig. 3a and 3b, respectively. Considering these 3 separate situations was necessary for imposing different boundary conditions to the model. Finally, the HCS was removed in case #4. With such geometrical description, the impacts of the presence of HCSs, of their floatability, and even of their thermal conductivity on the evaporation rate of water could be calculated.

3. Results and discussion

3.1. Carbonisation mechanisms and morphology of HCSs

The polymer capsules filled with the xylitol-erythritol mixture are shown in Fig. 6a. Their perfect spherical shape and well-defined diameter make them excellent templates for preparing HCSs. However, as explained in the previous section, hydrothermal carbonisation (HTC) was necessary before pyrolysis. A direct heat-treatment under nitrogen up to 900°C indeed made the capsules lose their spherical shape, undergo a considerable shrinkage, and stick to each other, although their hollow character was achieved, as seen in Fig. 6b.

Coating the polymer capsules with a carbon precursor in order to strengthen the final carbon shell and to maintain the spherical morphology was then carried out by HTC. During the process, the hydrochar derived from the various carbon precursors tested here (sucrose, tannin) preferentially deposited on the spherical templates and strengthened significantly their shells.

Moreover, the experimental conditions of such treatment (180°C, 24 h) allowed maintaining the spherical shapes of the templates, and the thickening of their shells allowed getting HCSs in good condition after pyrolysis at 900°C. Therefore, as mentioned above, the spherical hard templates used in this research were fully organic, and no inorganic matter had to be removed in a second step of the preparation process; the hollow character really emerged from the different carbon yields between core and shell materials upon pyrolysis. Only a significant shrinkage was observed: the diameter decreased by ~ 30% and by ~ 40% for big and small spheres treated in a solution of sucrose, respectively, corresponding to volume shrinkages of at least 60% and 80%, respectively. The result is shown in Fig. 6c. When the pyrolysis was carried out at 1500°C, the volume shrinkages were even higher, at least 70% and 85% for big and small spheres, respectively. The diameters of the HCSs prepared in various conditions are given in Table 2. Tannin as carbon precursor led to far lower shrinkage, most likely due to its higher carbon yield (see below).

In the experimental hydrothermal conditions, sucrose undergoes hydrolysis and thus produces glucose and fructose, catalysed by hydronium ions generated by water auto-ionisation. Then, those monosaccharides and/or their decomposition products undergo polymerisation or polycondensation reactions, producing soluble polymers [46]. The chemical mechanisms, detailed elsewhere [45], lead to hydroxymethylfurfural (5-HMF) molecules which polycondense and crosslink, engendering three-dimensional furanic structures. The latter grow by continuous dehydration of the 5-HMF monomer, become less and less hydrophilic, and finally precipitate. The nano-sized precipitates, around 5 nm in diameter and called “primary particles” [45] themselves tend to aggregate into larger carbonaceous spheres on the one hand, and condense onto the template on the other hand, forming a very rough shell as seen in Fig. 6d.

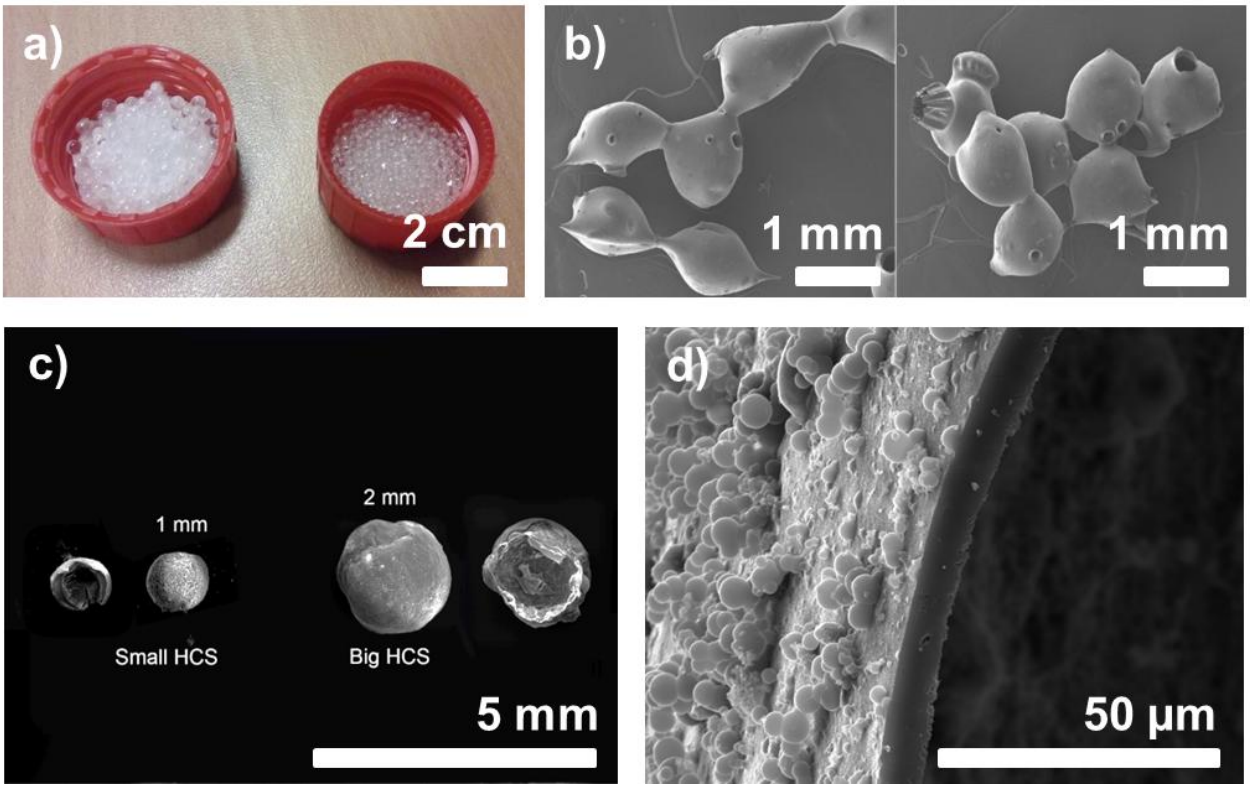

Fig. 6. (a) The two available sizes of polymer capsules filled with sugar alcohols used as templates for producing HCSs in this work: diameter ~ 2.6 mm (left) and ~ 1.8 mm (right); (b) Resultant materials after direct pyrolysis at 900°C of the small spheres shown in (a); (c) HCSs derived from small and big capsules shown in (a) after HTC in sucrose solution and pyrolysis at 900°C. A broken sphere is shown next to an intact one in each case to demonstrate the hollow character of the spheres; (d) Detail of the (broken) shell of one big HCS; the thickness is close to 10 µm.

Unlike sucrose, tannin is a natural polyphenol which, due to the presence of aromatic groups, proved to be another quite valuable source of carbon materials, leading to a relatively high carbon yield (45%, compared to 32% for sucrose) [52,53]. During HTC, tannin mainly undergoes autocondensation reactions based both on the opening of the O1-C2 bond of the flavonoid repeating unit (see again Table SI1 for the atom numbering) and on the subsequent condensation of the reactive centre formed at C2 with the free C6 or C8 sites of a flavonoid unit on another tannin chain [54,55].

Table 2. Parameters of HCSs, depending on the preparation conditions already detailed in Table 1 (size of templates, nature of carbon precursor, presence of metals, and pyrolysis temperature).

Sample name	Template	Precursor	M^{n+}	Pyrolysis T (°C)	Diameter (mm)	Oxygen content (wt.%)
PBS1.0C-900	Big	Sucrose	-	900	1.86±0.17	6.81
PBS1.0C-1500	Big	Sucrose	-	1500	1.72±0.19	4.51
PBT1.0C-1500	Big	Tannin	-	1500	2.14±0.14	3.51
PSS1.0C-900	Small	Sucrose	-	900	1.00±0.16	6.66
PSS1.0C-1500	Small	Sucrose	-	1500	0.92±0.11	3.74
PBSFeC-900	Big	Sucrose	Fe^{3+}	900	1.71±0.19	4.75
PBSFeC-1500	Big	Sucrose	Fe^{3+}	1500	1.55±0.25	2.53
PBSNiC-900	Big	Sucrose	Ni^{2+}	900	1.73±0.26	4.23
PBSNiC-1500	Big	Sucrose	Ni^{2+}	1500	1.63±0.23	2.19

3.2. Composition and carbon nanotexture of HCSs

During pyrolysis, it is expected that cyclisation and aromatisation reactions proceed, associated with the release of low-molecular-weight hydrocarbons, and followed by polycondensation of aromatic molecules. Generally speaking, around 600°C, mainly foreign atoms such as oxygen and nitrogen are generally released as CO_2, CO and $(CN)_2$, together with CH_4. Above 1000°C, the gas released is essentially H_2 as a result of the polycondensation of aromatics. Above 1300°C, the major part of foreign atoms, mainly hydrogen, goes out, and the residual solids are almost pure carbon materials. From the point of view of a nanotexture, during carbonisation, a preferred orientation of basic structural units based on hexagonal carbon layers is established.

However, when the temperature of pyrolysis is not high enough, carbon layers remain small and, in most cases, are stacked randomly (known as turbostratic structure). Especially when the thermosetting polymer precursors are heated very slowly (slower than the rate of the shrinkage to compensate the evolution of pores due to the release of decomposition gases from the precursor), the carbonised products shrink homogeneously, maintaining their morphology and giving glass-like carbons, which have a highly disordered nanotexture [56].

As a result, the composition of the materials becomes richer and richer in carbon when the pyrolysis temperature increases, and at the same time its nanotexture becomes less and less disordered. Given their precursors, the present HCSs only contain C, H and O, and their oxygen content was reported in Table 2. It can be seen that, as expected, higher pyrolysis temperatures led to less residual oxygen. Another interesting observation is that tannin produced HCSs with less oxygen than with sucrose. This fact is readily explained by the aromatic character of tannin and its lower oxygen content compared to sucrose, as clearly seen in Table SI1. Finally, metals acting as graphitisation catalysts (see below) produced the HCSs having the lowest O content, especially at higher pyrolysis temperature. Graphitic zones in the material indeed cannot incorporate oxygen in their structure, except at the edges of the aromatic layers, unlike more disordered carbon which contains a much higher proportion of sp^3 carbon atoms. It can even be observed that Ni, which is a better graphitisation catalyst than Fe (see below and [57 and refs. therein]), led to the lowest residual amounts of oxygen. It can therefore be anticipated that metal-loaded HCSs are the most hydrophobic but also those having the highest thermal conductivity, since the thermal conductivity of graphite (typically around 100 – 150 W m^{-1} K^{-1} for isostatic graphite, i.e., having randomly oriented crystallites [58]), is roughly ten times higher than that of sucrose-derived carbon pyrolysed at 900°C (around 10 W m^{-1} K^{-1} [59]).

When metal ions such as Fe(III) or Ni(II) were present during HTC, they were incorporated into the shell of the HCSs, and therefore the corresponding metals were dispersed in the carbon material after pyrolysis. The latter produced the partial reduction of Fe(III) into elemental iron and iron carbide (Fe_3C), and Ni(II) reduced into elemental nickel, as proved by the XRD patterns given in Fig. SI2. Metal-free materials are known to be non-graphitisable carbons, and indeed the XRD patterns of PBSC-900 proved that there is only amorphous carbon, even at a temperature of pyrolysis as high as 1500°C and whatever the carbon precursor, see Fig. SI2a.

Indeed, the typical two reflections (002) and (100) that indicate the graphitisation or not of carbon materials appear very broad, rather typical of a pitch, a highly aromatic precursor of synthetic graphite. When increasing the pyrolysis temperature, the (002) reflection became slightly narrower and shifted to higher Bragg angle (from 22.94° for PBS1.0C-900 to 23.72° for PBS1.0C-1500), thus corresponding to shorter repetition distances. The latter, however, being the interlayer spacing d_{002} (0.393 nm for PBS1.0C-900 and 0.359 nm for PBS1.0C-1500) are much higher than that of pure graphite, d_{002} = 0.335 nm. This might be due to intercalated oxygen functionalities and to less ordering in the carbon material. The XRD pattern of the material obtained from tannin as precursor (PBT1.0C-1500) was rather similar to the one obtained from sucrose, after pyrolysis at the same temperature, 1500°C, but a very broad (11*l*) reflection (gathering (110) and (112)) appeared at a Bragg angle around $2\theta = 80°$, suggesting a slightly less disordered material.

In contrast, the carbon nanotexture of iron-loaded HCSs appears much more ordered, as suggested by the corresponding XRD patterns shown in Fig. SI2b. To verify the improvement of the carbon ordering, these HCSs were treated at different temperatures: 900°C, 1200°C and 1500°C. Fig. SI2b thus proves the existence of both highly disordered carbon and graphite-like carbon. Especially, the (002) reflection became more intense and narrower as the pyrolysis

temperature increased, indicating the catalytic graphitisation effect of Fe, not observed without such catalyst. Iron particles were also detected by XRD. Their typical crystallite size, 30–35 nm, was calculated by application of Scherrer's equation: $\tau = \frac{K\lambda}{\beta\, cos\theta}$, where τ is the mean size of the ordered (crystalline) domains, K is a dimensionless shape factor, with a value close to unity (here 0.9), λ is the X-ray wavelength (here 0.15417 nm for Cu-Kα radiation), β is the line broadening at half the maximum intensity (FWHM) after subtracting the instrumental line broadening, in radians.

The reduced metal particles could also be observed on the SEM images shown in Fig. SI3. Big aggregates can be seen, i.e., far bigger than the crystallite size calculated from XRD results (see also Table SI2). As a result, the distribution of the metal in the carbon matrix was poorly homogeneous.

Nickel is also known to be a very good graphitisation catalyst [50,57]. Unlike the previous case of iron-loaded HCSs, the XRD patterns shown in Fig. SI4 indeed presented mostly flat baseline, suggesting the far lower amount of highly disordered carbon and thus the better catalytic graphitisation performances of Ni. It should be noticed that the (002) reflection of PBSNiC1500 was not as "sharp" as the others (see the inset of Fig. SI4), but might be divided into two peaks centred at 26.05° and 26.48°, respectively. The latter peak appeared at the highest pyrolysis temperature, and thus corresponds to a higher graphitisation level. Indeed, applying the empirical formula: d_{002} (nm) = 0.3354 g + 0.344 (1 - g) [60], where g^2 is the graphitisation degree (the closer to 1 is g^2, the higher is the graphitisation degree), one finds a graphitisation level of 66% for the 2nd peak, against 12% for the 1st one. The crystallite size, L_c, was also calculated from the same Scherrer's equation as before, and the corresponding microcrystalline structure analysis is given in Table SI2. Whether for Fe- or for Ni-loaded HCSs, the carbon crystallite size increased with

temperature, as expected, but was definitely higher with Ni. Table SI2 also evidences the lower interlayer spacing d_{002} in the presence of Ni. This finding further confirms the higher catalytic action of Ni for converting part of the carbon into a graphitic material. Finally, it can be seen from the SEM pictures shown in Fig. SI5 that the aggregated nickel particles were smaller than those of iron, but still were not homogeneously distributed all over the material.

XRD is a global analytical tool, whereas Raman spectroscopy is a very local one. Raman spectra of metal-free HCSs and Fe- and Ni-loaded HCSs were thus recorded at different, randomly chosen, zones of the materials. Fig. 7 and 8 show very representative examples, in which the spectra were not shifted with respect to each other for better visualising either that they are completely superimposed (Fig. 7 for metal-free HCSs), or on the contrary that they are very different from each other (some parts of Fig. 8 for metal-loaded HCSs). The present results thus confirmed the heterogeneity of metal-loaded HCSs, since the characteristics of either highly disordered or highly graphitised carbon could be obtained from one single HCS, depending on the position of the laser spot at the material's surface.

As for metal-free HCSs, Fig. 7a was obtained for one HCS prepared from big polymer beads used as templates onto which 1 g of sucrose was condensed in hydrothermal conditions, followed by pyrolysis at 900°C (PBS1.0C-900). Five investigated zones led to 5 identical spectra, suggesting the excellent homogeneity of the material in terms of carbon nanotexture. All full Raman spectra evidenced a first-order part, ranging from 1000 to 1800 cm^{-1}, presenting an intense and broad D band (around 1335 cm^{-1}) and a slightly narrower G band (around 1595 cm^{-1}) of rather similar intensity, and a second-order part, ranging from 2200 to 3400 cm^{-1}, which was very poorly structured. Such features are very typical of highly disordered carbons. Thus, the main band near 2700 cm^{-1} (S1 band) is known to split into two bands when the structure of carbon acquires a tri-

periodic order [61], i.e., involving an order in the way the carbon layers are stacked, which is obviously not the case here (Fig. 7a).

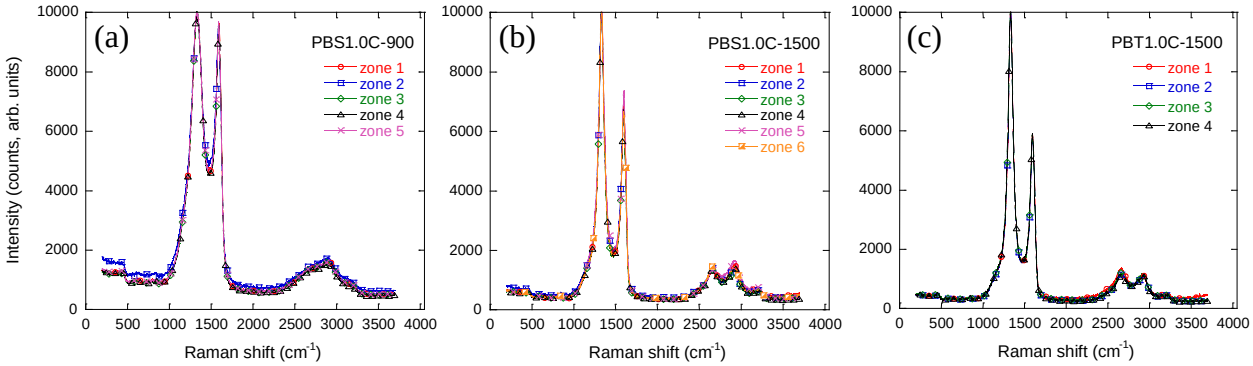

Fig. 7. Raman spectra of metal-free HCSs prepared from big-sized polymer beads and 1 g of sucrose after pyrolysis at: (a) 900°C; and (b) 1500°C. (c) Same as (b) but the HCSs were derived from tannin. The zones indicated on the figures are not the same from one plot to another.

HCSs prepared at 900°C but using tannin as the carbon precursor led to Raman spectra that were indistinguishable from those presented in Fig. 7a; therefore, those spectra are not shown here. The same applies to HCSs from sucrose prepared with the small-size capsule templates. However, some differences were observed once HCSs derived from sucrose or tannin were treated at 1500°C, see Fig. 7b and 7c. Whereas different zones from different spheres again led to highly reproducible spectra, supporting the homogeneity of these materials, the intensity ratio of D to G bands was clearly higher for HCSs derived from tannin. Since both sucrose and tannin chars are well-known non-graphitisable carbons in the absence of catalyst, an increase of the I(D)/I(G) ratio, where I is the maximum intensity of each band, indicates that these materials are in the carbonisation regime and not in the graphitisation regime [62]. In the graphitisation regime, the D/G ratio would decrease instead [63]. For those carbons that are non-graphitisable, the I(D)/I(G) ratio is expected to increase with L_a^2 [64], where L_a is the crystallite size along the carbon layers,

thus corresponding to the lateral extension of those crystallites. As a result, HCSs derived from tannin and treated at 1500°C possess larger crystallites and, consequently, less disordered nanotexture than HCSs derived from sucrose and treated at the same temperature. The appearance of two small peaks instead of a broad one in the 2nd-order part of the spectra (Fig. 7b and 7c) also confirmed the better organisation of the sucrose- or tannin-derived carbon treated at 1500°C.

Unlike for metal-free HCSs, the presence of iron led to very heterogeneous materials since 6 different investigated zones led to 6 different spectra, see Fig. 8a. Much more ordered zones (especially zones 1 and 6) were indeed observed near highly disordered zones (zone 3), the latter being identical to those observed in the absence of Fe. The action of Fe is particularly clear for zone 1, leading to the narrowest D and G bands and the highest intensity of the D band. Less ordered zones led to less intense peak at such wavenumbers, and to broader D and G bands. At the same time, the bands in the second-order region became more intense and more individualised, especially the S1 band. These findings suggest that the ‘‘catalytic graphitisation’’ reported here is therefore not a true graphitisation, but an improvement of the nanotexture still never reaching the usual triperiodic arrangement of graphite. The materials thus remained in the carbonisation regime and, despite their significantly increased atomic ordering, they did not enter the graphitisation regime [62].

The highly heterogeneous character of the samples was maintained when the pyrolysis temperature was increased to 1200°C, see Fig. 8b. Thus, highly disordered carbon was again observed (zone 6), but the “graphite-like” zones (especially zone 1) were even more ordered than at 900°C, due to the higher temperature of pyrolysis, as shown by the considerable increase of the second-order part of the spectra. Finally, at 1500°C, the effect was even more obvious, and all

spectra presented narrow bands and well-defined second-order parts. The samples also appeared to be more homogeneous since the spectra were much more reproducible, see Fig. 8c.

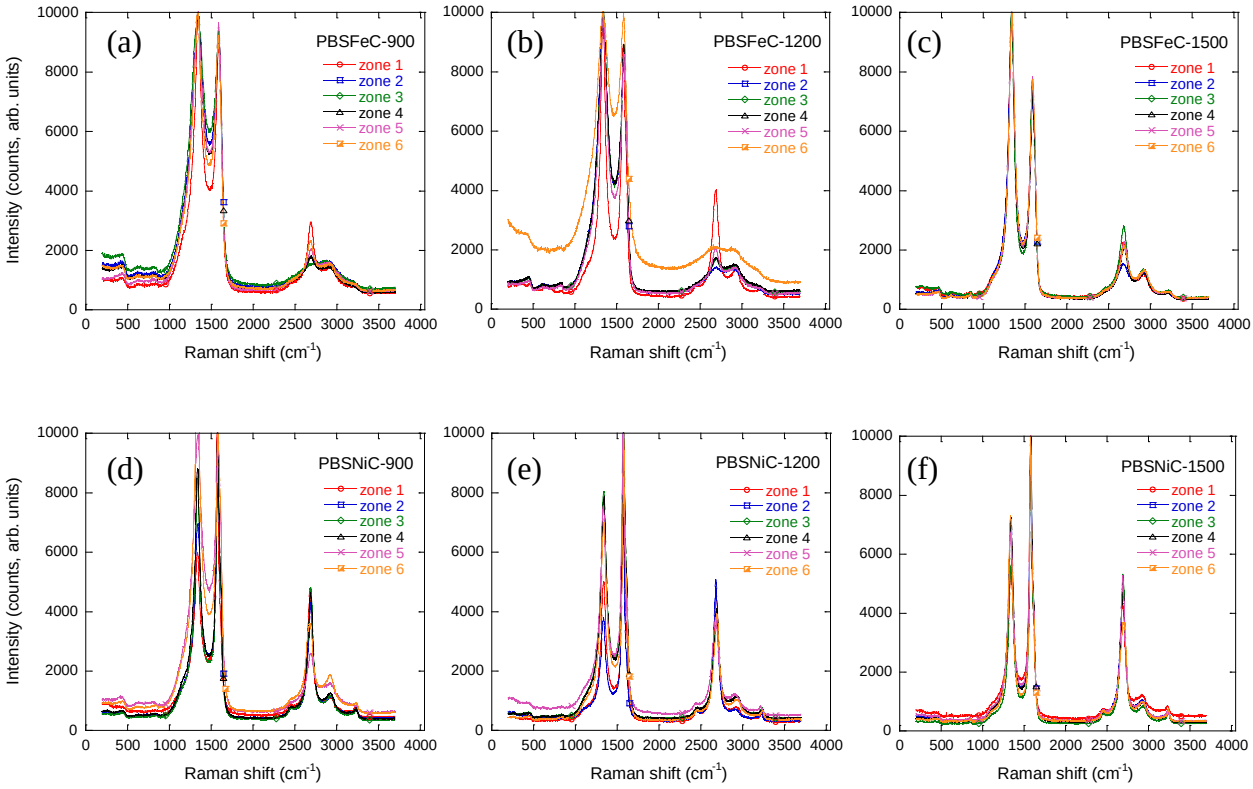

Fig. 8. Raman spectra of HCSs prepared from big-sized polymer beads and 1 g of sucrose in the presence of metals: (a, b c) Fe(III) at 0.1 mol L^{-1} or (d, e, f) Ni(II) at 1 mol L^{-1}, and after pyrolysis at three temperatures : (a, d) 900°C; (b, e) 1200°C; and (c, f) 1500°C. The zones indicated on the figures are not the same from one plot to another.

The same kinds of conclusions apply to materials obtained in the presence of nickel. However, in this case, the graphitisation was much more advanced as proved by the narrower bands, whatever the temperature of pyrolysis, and the far better structuration and intensification of the second-order part. Additionally, the G band increased significantly with the temperature of treatment until it became much higher than the D band. This suggests that the materials truly entered the graphitisation regime [62], a feature not observed with Fe as catalyst, for which only

band narrowing and a less extended increase of S1 band were evidenced. The corresponding spectra are presented in Fig. 8d-8f.

Generally speaking, the poor repeatability of Raman spectra of metal-loaded HCSs prevented their deconvolution into individual peaks able to account for the whole envelope of the spectra. Due to this, the usual calculation of reliable intensity ratios of D to G bands was not possible, although the trends were clearly observed. This problem is due to the fact that catalytic graphitisation proceeds when metal and carbon are in contact. Zones far from metal particles therefore remained highly disordered, whereas those near them were much more ordered and even efficiently graphitised in some cases. Therefore, the more efficient action of Ni as graphitisation catalyst might also be attributed to the higher concentration allowed by Ni(II) in the HTC process (1 mol L^{-1}) with respect to Fe(III) (0.1 mol L^{-1}).

3.3 Relevant properties of HCSs with respect to water evaporation rates

In order to be applicable as boosting objects for solar evaporation of water, HCSs are *a priori* expected to meet the following criteria:

a) They should be lightweight and hydrophobic enough for preventing their sinking in water;
b) However, they should not be too hydrophobic either so as to produce a sufficiently high interface area between the carbon shell and the water: a compromise should thus exist;
c) Their thermal conductivity should be *a priori* as high as possible;
d) They should be mechanically stable enough to avoid breakage while they float on the water and during potential recovery;
e) Ideally, they should possess a property allowing an as-easy-as-possible recovery.

In the following, the mechanical stability is addressed as well as how they can be collected after use. Next, the questions of wettability and floatability of HCSs are discussed.

Fig. SI6a shows three HCSs of type PBS1.0C-900 submitted to a reference weight of 50 g. The next heavier weight, 100 g, crushed the HCSs. Given the significant gap between these two weights, it was meaningless to test all kinds of HCSs in those conditions: trying the same with a few others indeed only produced the same result. Although all HCSs remain brittle materials, it must be stressed that each PBS1.0C-900 weighs around 0.5 mg, and therefore the experiment shown in Fig. SI6a suggests that each of them was able to withstand 33 000 times its own weight. This is far enough for the intended application, for which no stress is applied to floating HCSs.

It should be noticed that the metals gave HCSs a strong magnetic character, as seen in Fig. SI6b, which can be quite useful for an easy and fast recovery of the materials after use. Such feature only appeared after pyrolysis, i.e., once Fe(III) and Ni(II) cations (which are paramagnetic) were reduced by carbon into elemental Fe and Ni (which are ferromagnetic metals, hence with a far higher magnetic susceptibility), respectively, at 900°C.

Representative results of water contact angle (WCA) measurements are presented in Fig. SI7. The correction method explained in Fig. SI1a, tested with two kinds of HCSs, proved to be poorly accurate due to the geometrical uncertainties already mentioned in section 2.2. However, despite these uncertainties, consistent behaviours could be evidenced, as seen in Fig. SI7a-SI7b, and the material made of tannin and pyrolysed at the highest temperature (PBT1.0C-1500) was visibly less hydrophilic (after a given equilibration time) than the one made of sucrose and pyrolysed at 900°C. This finding is in complete agreement with what was expected from the studies of carbon nanotexture and composition.

The method based on curved baseline shown in Fig. SI1b led to the same behaviour, as seen in Fig. SI7c-SI7d, but with an improved quality of the measurements: whatever the time after deposition of the droplet, no crossover was seen, and the values of WCA were better differentiated. For this reason, only this method was tested with other HCSs. Not all families were investigated because it was quickly concluded that wettability alone was not the key parameter for understanding the different performances of HCSs in terms of solar evaporation rate. More data are presented in Fig. SI8, and it indeed appeared that neither the most hydrophilic nor the most hydrophobic HCSs were the best materials for this application (see next section). Additionally, some counterintuitive though reproducible results were observed. For instance, whereas Ni- and Fe-loaded materials pyrolysed at 900°C contained similar amounts of oxygen (see again Table 2), and whereas the graphitisation was higher in the case of Ni-loaded HCSs, the latter were by far the most hydrophilic and the Fe-loaded ones were the most hydrophobic. It had to be concluded that the observed effect were rather due to the roughness of the carbon shells, indeed much higher for Fe-loaded HCSs, than to the surface chemistry or to its nanotexture. The surface of Ni- and Fe-loaded HCSs treated at 1500°C was even so rough that no repeatable water contact angle could be measured. The floatability was thus considered instead.

Such difference of behaviour between Ni- and Fe-loaded HCSs pyrolysed at 900°C was observed at the moment of installing these materials at the surface of water: those loaded with Ni quickly adopted the stable configuration shown in Fig. 3b, whereas the ones containing Fe easily adopted the minimal wetting configuration of Fig. 3a for a long time. Moving vigorously the water covered by those HCSs forced them to be wetted so that they could finally adopt the maximal wetting configuration. Other HCSs such as PBS1.0C-1500 for instance presented an intermediate

behaviour. The corresponding results are shown in Fig. 9 for the two cases of minimal and maximal wetting, as a function of the HCS apparent density.

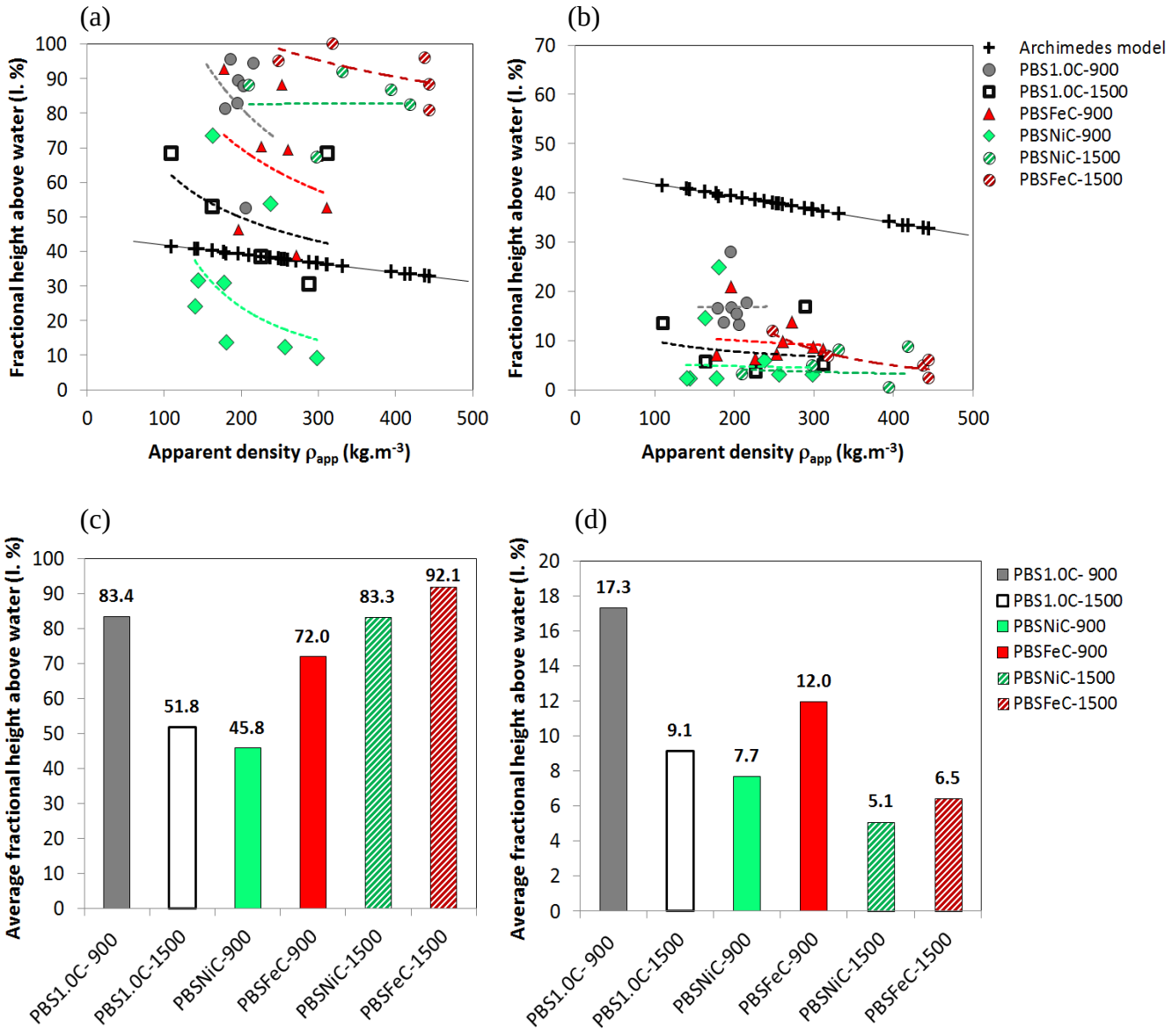

Fig. 9. Fraction of diameter above the water level of floating HCSs from 3 different families in the case of: (a) minimal wetting; and (b) maximal wetting. The straight line on the plots corresponds to the position of floating bodies in the same range of apparent densities, calculated from Archimedes' principle, i.e., in the absence of surface tension effect (see text). (c) and (d) correspond to averaged data for the HCS families shown in (a) and (b), respectively.

The general observed trend is that the fraction of diameter above the water level decreased when the apparent density of the HCSs increased, as expected from the effect of gravity. In agreement with the results presented in Fig. SI8, the Fe-loaded HCSs treated at 900°C floated far above the water level with respect to Ni-loaded ones treated at the same temperature in the case of minimal wetting, but such difference was much lower in the stable configuration of maximal wetting. In the case of minimal wetting (Fig. 9a), all tested HCSs except most of PFSNiC-900 float above what can be calculated from the Archimedes' principle applied to spheres whose apparent densities are in the range measured here, i.e., in the absence of surface tension effects. The difference between experimental results and those calculated from Archimedes' principle thus suggest that Ni-based HCSs are wetted, whereas the others are not. After forced wetting (Fig. 9b), all HCSs have their diameter well below the level of what was calculated from Archimedes' principle, suggesting that all are hydrophilic, although to various extents. Moreover, the relative positions of some families of HCSs with respect to others changed from minimal to maximal wetting, as observed in Fig. 9c and 9d, showing the average positions of each family of HCS. This is especially the case for the materials PBSFeC-900, PBSNiC-1500 and PBSFeC-1500, which were floating far above the liquid level when gently placed at the surface of salt water, but soaked the most after forced wetting. This finding might be explained by the very rough surface observed for these materials, producing a kind of Lotus effect in the metastable configuration but also a surface porosity making them much more wetted after forced imbibition.

Based on these results, if the capacity of the HCSs to boost the evaporation of salt water was related to the fraction of material immersed in the liquid, on would get the order:

PBSNiC-900 > PBSC-1500 > PBSFeC-900 > PBSNiC-1500 > PBSC-900 > PBSFeC-1500 (10)

in the metastable configuration, and:

PBSNiC-1500 > PBSFeC-1500 > PBSNiC-900 > PBSC-1500 > PBSFeC-900 > PBSC-900 (11)

in the stable configuration. Given that only the latter was considered for long-term evaporation test, then Eq. (11) should be the relevant one for explaining the various performances of the HCSs.

3.4. Impact of HCSs properties on the evaporation rate of salt water

The previous results thus suggest that, rather than the natural hydrophobicity of aromatic carbon, the hollow character of HCSs and hence their correspondingly low apparent density allow them to float over the water surface for quite long times, as illustrated in Fig. SI9a. Fig. SI9b shows the weight loss of a beaker containing 20 g of 3.5 wt.% NaCl and submitted to a radiant power of 1 kW m^{-2} as a function of time. The observed weight loss was linear over the considered period, and the slope of the linear fit led to the evaporation rate. The same was repeated at different radiant densities and in the presence of various kinds of HCSs. As seen below, and generally speaking, HCSs improved the solar evaporation rate, which further increased by increasing the power density of the sunlight simulator. As for the data of Fig. SI9b, it can be observed that, on average, the evaporation rates in the absence of HCSs were roughly 3 – 5 times higher than what was reported in former studies [4, 65], in which no forced convection was used. Such difference will be confirmed by our value of convective exchange coefficient, typically 5 times higher than what is usually found for natural convection (see next section below).

Raw data of evaporation rates as a function of radiant power density are given in Fig. 10 for salt water evaporation in the absence of HCSs and in the presence of big and small HCSs pyrolysed at either 900°C (PBS1.0C-900 and PSS1.0C-900, Fig. 10a) or 1500°C (PBS1.0C-1500 and PSS1.0C-1500, Fig. 10b), i.e., allowing to compare the influence of the size of HCSs and the effect of their pyrolysis temperature.

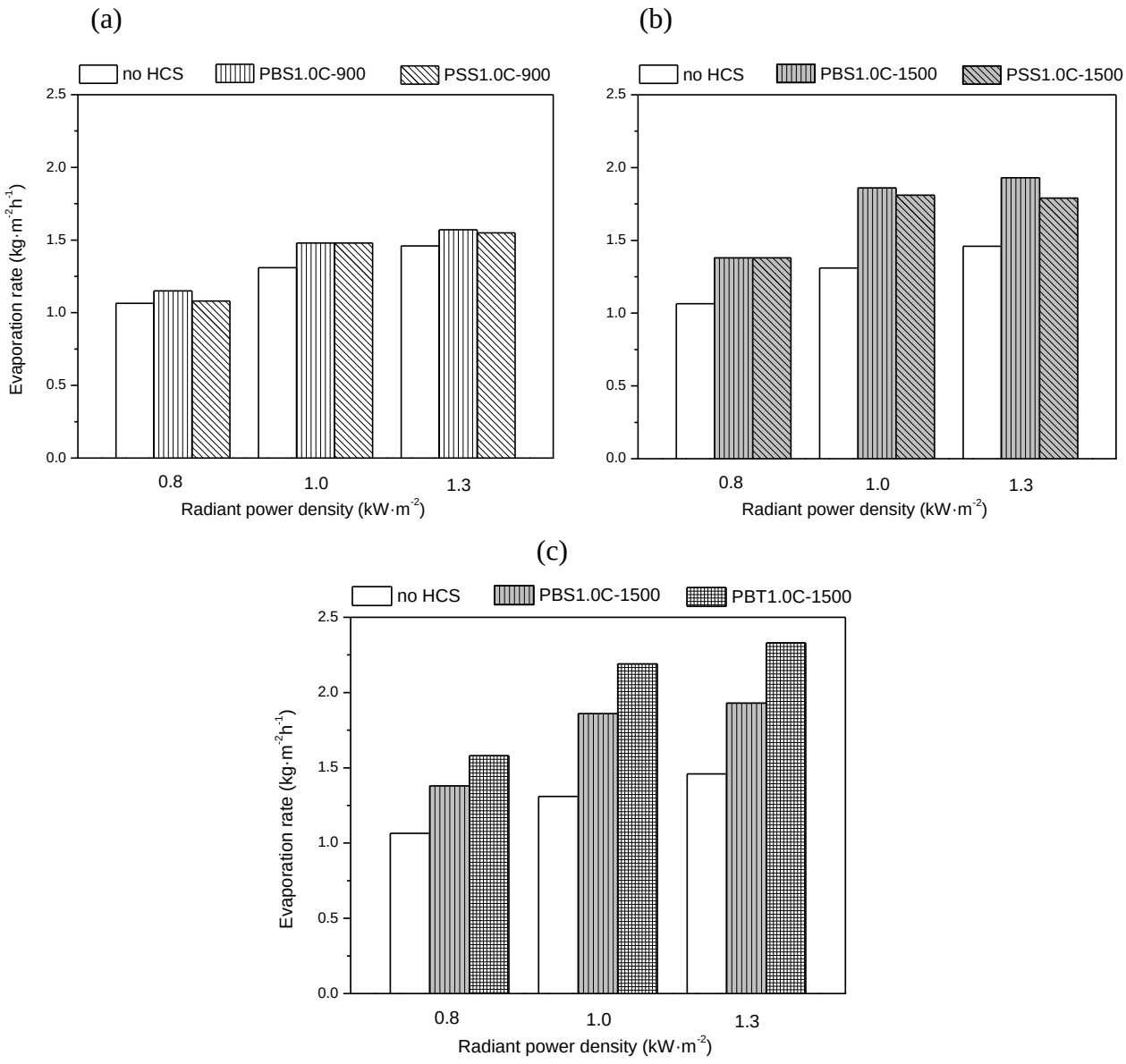

Fig. 10. (a) Evaporation rate of big (PBS1.0C-900) and small (PSS1.0C-900) HCSs derived from sucrose and pyrolysed at 900°C, compared to the HCS-free reference; (b) same as (a) but the HCSs were pyrolysed at 1500°C (PBS1.0C1500 and PSS1.0C1500); (c) same as (b) but for big HCSs derived from sucrose (PBS1.0C-1500) and from tannin (PBT1.0C-1500), both pyrolysed at 1500°C. The average diameters of all those HCSs have been given in Table 2.

Fig. 10a indicates that the small HCSs are rather poorly effective, or at least less efficient than the big ones treated at the same temperature (900°C); this effect is more easily seen under the highest tested power density of 1.3 kW m^{-2}. The higher performances of big HCSs is even more

obvious in Fig. 10b, corresponding to materials treated at 1500°C, and especially again under the highest radiant flux.

These results might not be directly related to the average size, since the surface fraction of identical spheres arranged in a two-dimensional close-compact packing remains the same, whatever their diameter. The observed difference should thus rather be explained by the observed broader distribution of sizes of the small HCSs, leading to a more defective and less compact floating monolayer, and/or by the slightly higher oxygen content of bigger HCSs compared to small ones, as revealed in Table 2. A higher O content should be related to a lower hydrophobicity and hence to a higher contact area between HCSs and water. This is especially true for HCSs treated at 1500°C, for which the smaller spheres have a lower O content than bigger ones (3.74 vs 4.51%, respectively), and hence lead to a lower evaporation rate. Such trend was observed for all HCSs, as seen in Fig. SI10a in which linear fits were drawn for each radiant power. A slightly hydrophilic character can indeed help forming a thin layer of water on the top surface of HCSs and promote capillary forces and imbibition [38]. Hydrophobicity thus appears as a necessary condition for having HCSs that are not completely filled with water and don't sink after a given time, but a too high hydrophobicity would limit the contact with water and thus the transfer of solar heat to the water. As a result, an optimum water contact angle seems to exist, as shown in Fig. SI10b.

Fig. 10c shows the evaporation rate of big HCSs derived from sucrose and tannin after pyrolysis at 1500°C. Under the three tested irradiation conditions, tannin as carbon precursor is better for enhancing the evaporation. This might be due to the fact that tannin is a polyphenolic compound that can lead to higher content of more aromatic and more organised carbon in the final material, as seen by Raman spectroscopy. Consequently, one might expect higher thermal

conductivity and thus better heat transfer towards water. Moreover, the water contact angles were found to be very similar and close to the optimum suggested by Fig. SI10b (50.0° and 50.9° in tannin-derived and sucrose-derived HCSs, respectively), whereas their oxygen content was not very different either (3.51 wt.% and 4.51 wt.% in tannin-derived HCSs and sucrose-derived HCSs, respectively), considering the typical uncertainty of elemental analysis (± 0.5 wt.%). However, the modelling below will show that the effect of thermal conductivity is totally negligible, so the main difference between PBS1.0C-1500 and PBT1.0C-1500 should be explained in terms of differences of floatability. The combined result of oxygen content, carbon aromaticity and roughness, and apparent density of the HCSs leads to some changes of floatability, presented in Fig. SI10c as a function of contact angle in the cases of minimal and maximal wetting. Even if the scattering of the results is not negligible, and even if some data are missing because of the impossibility of getting them experimentally, clear trends can be seen: the more the HCSs are wetted, the less is their height fraction floating above the water level. The results obtained with metal-loaded HCSs (below) confirm that floatability controls the evaporation rate.

The aim of loading HCSs with Fe and Ni was double: (i) making them magnetic for an easy recovery from the surface of water, and (ii) making them partly graphitised for an expected increase of thermal transfer towards water. Table 2 confirmed that the metal-loaded HCSs have a lower oxygen content compared to metal-free ones, when pyrolysed at the same temperature. Figs. 11a and 11b show the evaporation rate of the HCSs pyrolysed at 900 and 1500°C, respectively. Fig. 11a indicates that, on average, an enhancement of solar evaporation rate was observed when going from metal-free HCSs pyrolysed at 900°C (PBS1.0C-900) to Fe-loaded (PBSFeC-900) and to Ni-loaded (PBSNiC-900) materials. The maximum enhancement appeared for PBSNiC-900 under 1.3 kW m^{-2}, and corresponded to around 30% of increase with respect to salt water alone.

For the HCSs pyrolysed at 1500°C, see Fig. 11b, the metal-free HCSs (PBS1.0C-1500) and the Ni-loaded (PBSNiC-1500) ones showed better performances compared to Fe-loaded HCSs (PBSFeC-1500). And the maximum enhancement appeared for PBSNiC-1500 under 1.3 kW m^{-2}, leading to an evaporation rate about 70% higher than that of salt water alone. It also appeared that metal-free HCSs prepared from tannin at the same temperature are almost as efficient (see again Fig. 10c).

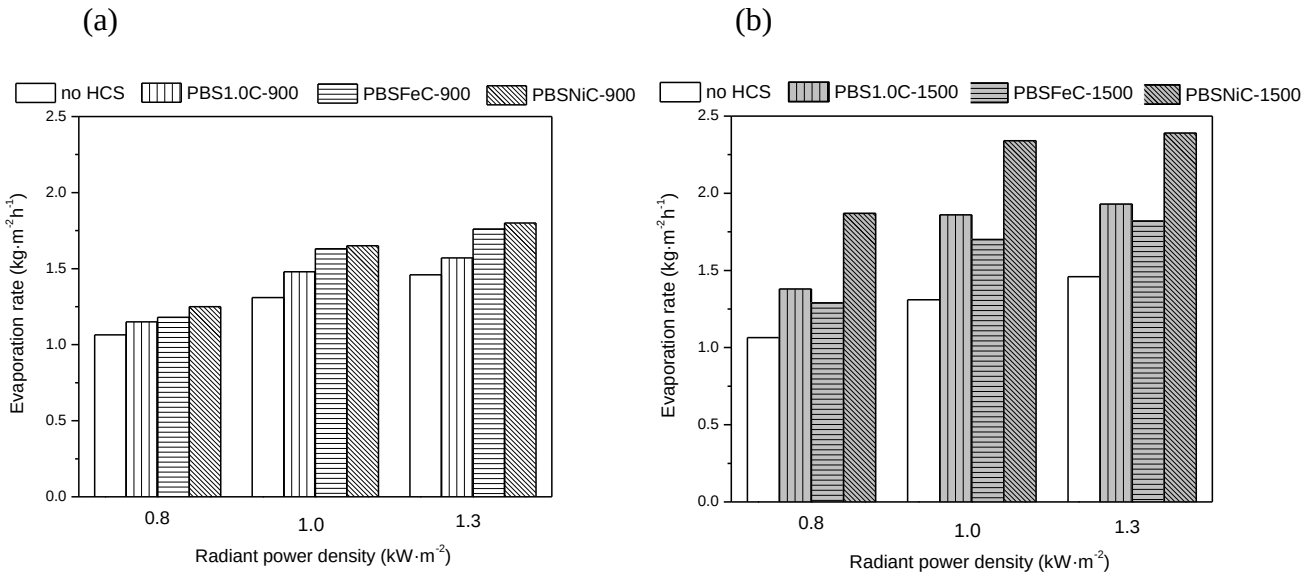

Fig. 11. (a) Evaporation rate of big HCSs derived from sucrose, either metal-free (PBS1.0C-900) or loaded with Fe (PBSFeC-900) or Ni (PBSNiC-900), and pyrolysed at 900°C; (b) same as (a) but for HCSs pyrolysed at 1500°C.

Gathering all results presented in Fig. 10 and 11, it can be seen that the evaporation rate is directly correlated to the floatability of the HCSs whatever the radiant power considered, as shown in Fig. 12. The order given in Eq. (11) is obeyed with only one exception, suggesting once more that floatability is indeed the parameter controlling the evaporation performances of HCSs, and that the expected increase of their thermal conductivity after partial graphitisation of their shell has

a negligible impact on their performances for water evaporation. Modelling was carried out for definitely confirming those findings.

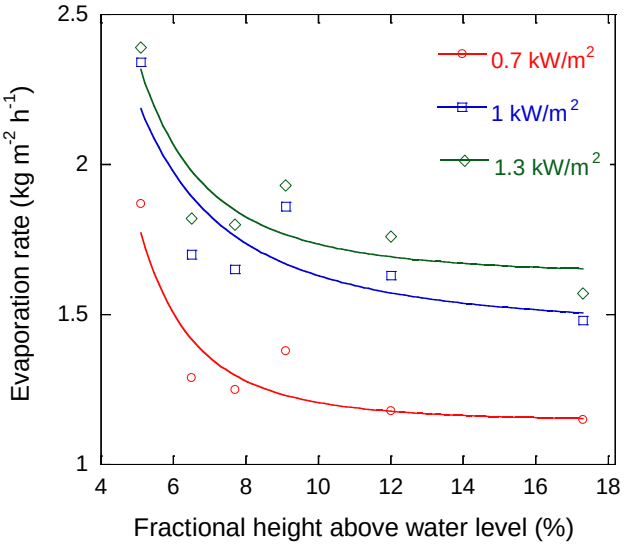

Fig. 12. Evaporation rate of HCSs submitted to 3 different radiant powers, as a function of their fractional height floating above the water level. The curves are just guides for the eye.

3.5. Predictions from the modelling

The evaporation flow rate in the absence of radiant flux was first estimated from the data of Fig. 10, in which the evaporation rates of HCS-free salt water submitted to various radiant powers were given. Assuming a linear phenomenon, the evaporated mass after 1h was thus extrapolated at zero radiant flux, and found to be 0.64 kg m^{-2}. The model without HCS was then applied in order to recover such value, and the corresponding convective exchange coefficient was found to be h_c = 47 W m^{-2} K^{-1}. Such value is within the standard range reported for forced convection, and is typically 5 times higher than what is usually found for natural convection, around 10 W m^{-2} K^{-1} [66].

Based on the value of h_c under forced convection conditions, the water evaporation rate of the HCS-free system was calculated as a function of time with a radiant power of 1 kW m^{-2}, but the results were found to be lower than our measurements, as seen in Fig. SI11. This suggests either that the system absorbs part of the radiant heat flux (assuming that the temperature of air is constant), or that the temperature of air increases. The source term P_{abs} defined by Eq. (2), and which allows taking the solar energy into account, was assumed to increase linearly with the power of the solar simulator, i.e.:

$$P_{abs} = \alpha P_{surf} \tag{12}$$

where P_{abs} (W m^{-3}) is again the volume power absorbed by water, P_{surf} (W m^{-2}) is the power received at the surface, and α (m^{-1}) is a proportionality constant. The corresponding fit to the experimental data is shown in Fig. SI11, and led to $\alpha = 40$.

The calculations for the four cases shown in Fig. 5b were then carried out, considering one HCS of diameter 1 mm whose position was shifted from 15 mm below the water level to 0.45 mm above the water level. The position zero mm thus corresponds to an HCS whose waterline passes through its centre. The results are presented in Fig. 13. It can be seen that, by moving the HCS upwards, the evaporation flow rate first progressively increases as long as the situation corresponds to case #1 of Fig. 5b (i.e., with HCS positions ranging from -15 mm to -0.5 mm). Then, moving to case #2 (i.e., with HCS positions ranging from -0.5 mm to 0 mm), the evaporation flow rate suddenly drops and presents a minimum at 0 mm, where the sphere has one half emerged and the other half under the water level. Finally, moving to case #3 (i.e., with HCS positions ranging from 0 mm to 0.45 mm), the evaporation flow rate increases sharply again but with values that remain lower than those of sunken HCS at moderate depths (i.e., at positions ranging from -13 mm to -0.5 mm).

The observations are explained both by the variations of exchange area between the water and the atmosphere and by the ability of the HCS to absorb the radiant heat. The exchange area is the lowest when exactly one half of the HCS is inside/outside the water, thus explaining the minimum of evaporation rate at the position 0 mm. At the position -0.5 mm, at which the full HCS is below the water level but still in contact with its surface, the evaporation rate is the highest because: (i) the area available for evaporation is the highest, and (ii) the HCS touches the surface and can thus absorb most of the radiant flux, increase locally its temperature and therefore heat the water by conduction. Looking again at Eq. (9), it can be seen that the surface evaporation flow rate depends on the difference of temperature between air and water surface on the one hand, and on the p_v/T ratio on the other hand, the latter being itself dependent on the surface temperature. If the surface temperature increases due to the presence of one HCS, then p_v/T also increases and so does the evaporation mass flux (F_m in Eq. (7)). The impact of the presence of one HCS in the presently modelled system of water column with a square cross-section of side 1 mm is clearly shown in Fig. SI12: the surface temperature, the vapour pressure and the p_v/T ratio are all significantly higher with HCS than without HCS.

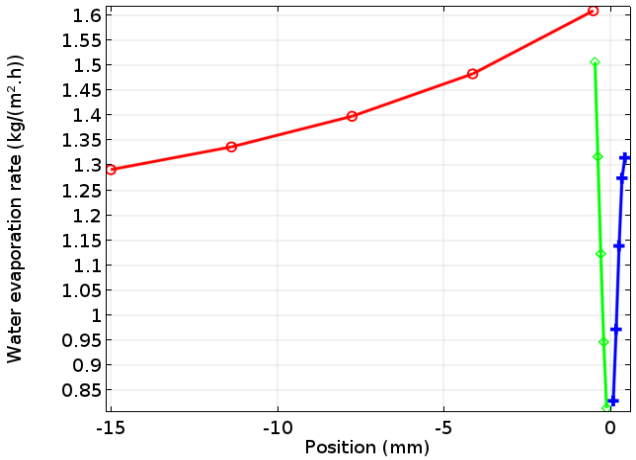

Fig. 13. Calculated evaporation rate after one HCS (diameter 1 mm) was introduced in the system (water column of square cross-section with side 1 mm) submitted to a radiant flux of 1 kW m^{-2}, as

a function of the HCS position. The colour codes corresponding to cases #1, #2, and #3 are the same as in Fig. 5b.

In [4], the authors highlighted the effect of the thermal conductivity of the HCSs: the higher was the thermal conductivity, the higher was the evaporation rate. However, the way they obtained the thermal conductivity of their HCSs can be criticised (a pellet, necessarily porous and poorly consolidated, was made, and the conductivity was recalculated from laser flash measurements, which needs some assumptions on the value of ρC_p) and, moreover, no such effect could be observed here. To estimate the range to be explored, the thermal conductivity λ of one single HCS was calculated from the equation of Gibson and Ashby which holds for purely closed-cell foams near room temperature, i.e., for which the contribution of radiative transfer can be neglected [67]:

$$\lambda = \frac{2}{3}(1-\Phi)\lambda_s + \Phi\,\lambda_g \qquad (13)$$

In Eq. (13), λ_s and λ_g (W m^{-1} K^{-1}) are the thermal conductivities of the solid and of the gas (air), respectively, and Φ (dimensionless) is the volume fraction of air in the HCS. λ_g was fixed at 0.026 W m^{-1} K^{-1}, whereas the values given in section 3.2 for isostatic graphite (100 - 150 W m^{-1} K^{-1}) and for sucrose-derived carbon pyrolysed at 900°C (10 W m^{-1} K^{-1}) were tested. The value of Φ was obtained by considering a HCS of diameter 1 mm and shell thickness 10 µm, so that Φ = 94.12%. Therefore, Eq. (13) suggests that the thermal conductivity of a HCS made of either pure sucrose-derived carbon treated at 900°C or pure isostatic graphite should range from ~ 0.4 to ~ 4-6 W m^{-1} K^{-1}, respectively.

This range, which is already unrealistically broad, was widened further to 0.2 – 10 W m^{-1} K^{-1}, and those extreme values were tested. The results are shown in Fig. 14. It can be seen that the impact of the thermal conductivity is quite low since a change of less than 10% was obtained. This

finding definitely suggests that the effect observed by Zhou et al. [4] was not attributable to some differences of thermal conductivity but to another physical properties of their HCSs, since the authors could only multiply the conductivity by a factor 1.23 (against 500 in the simulation) by changing the composition of their materials.

Finally, our first assumption in section 2.4 according to which the radiation absorbed by water is considered as a source term proportional to the incident radiation, was also tested. Such source term was thus set to zero and the evaporation rate was recalculated for the same two extreme values of thermal conductivities considered above. The results, shown in Fig. SI13, clearly evidence that the impact of thermal conductivity is negligible. Therefore, it is reasonable to conclude that the main factor influencing the water evaporation rate is the floatability of the HCSs rather than their thermal conductivity.

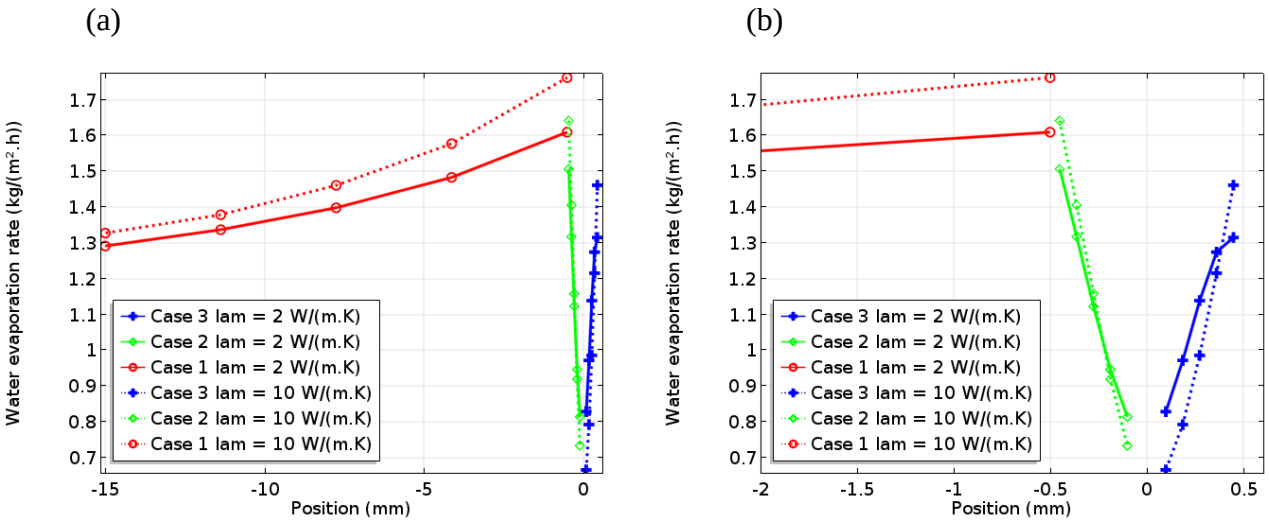

Fig. 14. Calculated change of evaporation rate as a function of the position of the HCS, for two extreme values of its thermal conductivity, λ ("lam" on the plots). (b) is a zoom of (a) in the range of positions where the water evaporation changes the most.

4. Conclusion

In this work, hollow carbon spheres (HCSs) were produced from sugar alcohols encapsulated in photocurable polymer shells. Such polymer capsules were prepared with two different diameters but none could survive direct pyrolysis. For using them as templates and producing HCSs, a preliminary hydrothermal treatment was necessary, using hot pressurised solutions of either sucrose or tannin used as carbon precursors. The latter indeed deposited on the polymer shell and stabilised the spherical capsules. After drying the resultant materials, pyrolysis was carried out at either 900 or 1500°C, leading to HCSs. The hydrothermal treatment also allowed loading those HCSs with metals, and Fe(III) or Ni(II) salts were used for that purpose.

As a result, various HCSs were obtained, having different sizes, various residual oxygen contents, and based on more or less disordered carbon. The materials containing metals presented a strongly magnetic character, and those loaded with Ni were clearly graphitised, especially when treated at the highest temperature, as proved by both XRD and Raman spectroscopy. All these differences were expected to have various impacts on the properties of the HCSs, especially in terms of water contact angle, floatability, and thermal conductivity.

When tested as light-absorbing materials floating at the surface of salt water (mimicking seawater) for interfacial solar heating, i.e., involving absorption and conversion of solar energy into heat at the water-air interface, it was unambiguously shown that these HCSs could enhance the solar water evaporation by up to 70% under a radiant power density of 1.3 kW m^{-2} under conditions of forced convection. The enhancement performance of the HCSs varied depending on the diameter, precursor, presence of metal, and pyrolysis temperature. It was conjectured that an optimum exists between a too high hydrophobicity, making the HCSs float far above the waterline, and a too high hydrophilicity, making them sink, and it was observed that the balance

between these limits is a complex combination of contributions from apparent density, oxygen content, graphitic character, and wettability of HCSs.

All these properties were successfully accounted for at once by considering the floatability of the HCSs, measured as their fractional height above the water level. Modelling the water evaporation confirmed the major effect of floatability, the highest efficiency being obtained when full HCSs are below the water level but still in contact with the water surface, and the negligible effect of their thermal conductivity.

Acknowledgements

The authors gratefully acknowledge the financial support of the CPER 2007–2013 "Structuration du Pôle de Compétitivité Fibres Grand'Est" (Competitiveness Fibre Cluster, France), through local (Conseil Général des Vosges), regional (Région Lorraine), national (DRRT and FNADT) and European (FEDER, France) funds.

References

[1] Li S, Pasc A, Fierro V, Celzard A. Hollow carbon spheres, synthesis and applications – a review. J. Mater. Chem. A 2016; 4(33):12686-713.

[2] Shen J, Li J, Chen Q, Luo T, Yu W, Qian Y. Synthesis of multi-shell carbon microspheres. Carbon 2006; 44(1):190–3.

[3] Sun Z, Song X, Zhang P, Gao L. Template-assisted synthesis of multi-shelled carbon hollow spheres with an ultralarge pore volume as anode materials in Li-ion batteries. RSC Adv. 2015; 5:3657-64.

[4] Zhou J, Sun Z, Chen M, Wang J, Qiao W, Long D, et al. Macroscopic and mechanically robust hollow carbon spheres with superior oil adsorption and light-to-heat evaporation properties. Adv. Funct. Mater. 2016; 26:5368–75.

[5] Cui HG, Cai JK, Zhao H, Yuan B, Ai C, Fu ML. Rapid and efficient fabrication of multilevel structured silica micro-/nanofibers by centrifugal jet spinning. J. Colloid Interface Sci. 2014; 425:131–5.

[6] Chang B, Shi W, Guan D, Wang Y, Zhou B, Dong X. Hollow porous carbon sphere prepared by a facile activation method and its rapid phenol removal. Mater. Lett. 2014; 126:13–6.

[7] Ji Q, Yoon SB, Hill JP, Vinu A, Yu JS, Ariga K, Layer-by-layer films of dual-pore carbon capsules with designable selectivity of gas adsorption. J. Am. Chem. Soc. 2009; 131(12): 4220–1.

[8] Nongwe I, Ravat V, Meijboom R, Coville NJ. Efficient and reusable Co/nitrogen doped hollow carbon sphere catalysts for the aerobic oxidation of styrene. Appl. Catal., A, 2013; 466:1–8.

[9] Ravat V, Nongwe I, Coville NJ, Palladium-supported boron-doped hollow carbon spheres as catalysts for the solvent-free aerobic oxidation of alcohols. ChemCatChem 2012; 4(12):1930–4.

[10] Mezzavilla S, Baldizzone C, Mayrhofer KJJ, Schüth F. General method for the synthesis of hollow mesoporous carbon spheres with tunable textural properties. ACS Appl. Mater. Interfaces 2015; 7(23):12914–22.

[11] Hu FP, Wang Z, Li Y, Li C, Zhang X, Shen P.K. Improved performance of Pd electrocatalyst supported on ultrahigh surface area hollow carbon spheres for direct alcohol fuel cells. J. Power Sources, 2008;177(1):61–6.

[12] Yan J, Meng H, Xie F, Yuan X, Yu W, Lin W, et al. Metal free nitrogen doped hollow mesoporous graphene-analogous spheres as effective electrocatalyst for oxygen reduction reaction. J. Power Sources 2014; 245:772–8.

[13] Zhang WM, Hu JS, Guo YG, Zheng SF, Zhong LS, Song WG, et al. Tin-nanoparticles encapsulated in elastic hollow carbon spheres for high-performance anode material in lithium-ion Batteries. Adv. Mater. 2008; 20(6):1160–5.

[14] Zhong Y, Wang S, Sha Y, Liu M, Cai R, Li L, et al. Trapping sulfur in hierarchically porous, hollow indented carbon spheres: a high-performance cathode for lithium–sulfur batteries. J. Mater. Chem. A 2016; 4:9526–35.

[15] Jayaprakash N, Shen J, Moganty SS, Corona A, Archer LA. Porous hollow carbon@sulfur composites for high-power lithium-sulfur batteries. Angew. Chem., Int. Ed. 2011; 50(26):5904–8.

[16] Ferrero GA, Fuertes AB, Sevilla M. N-doped porous carbon capsules with tunable porosity for high-performance supercapacitors. J. Mater. Chem. A 2015; 3:2914–23.

[17] Cai T, Xing W, Liu Z, Zeng J, Xue Q, Qiao S, et al. Superhigh-rate capacitive performance of heteroatoms-doped double shell hollow carbon spheres. Carbon 2015; 86:235–44.

[18] Bhattacharjya D, Kim MS, Bae TS, Yu JS. High performance supercapacitor prepared from hollow mesoporous carbon capsules with hierarchical nanoarchitecture. J. Power Sources, 2013;244:799–805.

[19] Portet C, Yang Z, Korenblit Y, Gogotsi Y, Mokaya R, Yushin G. Electrical double-layer capacitance of zeolite-templated carbon in organic electrolyte. J. Electrochem. Soc. 2009; 156(1):A1–A6.

[20] Murali S, Dreyer DR, Valle-Vigón P, Stoller MD, Zhu Y, Morales C, et al. Mesoporous carbon capsules as electrode materials in electrochemical double layer capacitors. Phys. Chem. Chem. Phys. 2011; 13:2652–5.

[21] Fang B, Kim JH, Kim M-S, Bonakdarpour A, Lam A, Wilkinson DP, et al. Fabrication of hollow core carbon spheres with hierarchical nanoarchitecture for ultrahigh electrical charge storage. J. Mater. Chem. 2012; 22:19031–8.

[22] Yuan C.Q, Liu XH, Jia MY, Luo ZX, Yao JN. Facile preparation of N- and O-doped hollow carbon spheres derived from poly(*o*-phenylenediamine) for supercapacitors. J. Mater. Chem. A 2015; 3: 3409–15.

[23] Xu J, He F, Gai S, Zhang S, Li L, Yang P. Nitrogen-enriched, double-shelled carbon/layered double hydroxide hollow microspheres for excellent electrochemical performance. Nanoscale 2014; 6:10887–95.

[24] Yoon SB, Sohn K, Kim JY, Shin C-H, Yu J-S, Hyeon T. Fabrication of carbon capsules with hollow macroporous core/mesoporous shell structures. Adv. Mater. 2002; 14(1):19–21.

[25] Kim M, Yoon SB, Sohn K., Kim JY, Shin C-H, Hyeon T, et al. Synthesis and characterization of spherical carbon and polymer capsules with hollow macroporous core and mesoporous shell structures. Microporous Mesoporous Mater. 2003; 63(1-3):1–9.

[26] Wu C, Zhu X, Ye L, OuYang C, Hu S, Lei L, et al. Necklace-like hollow carbon nanospheres from the pentagon-including reactants: synthesis and electrochemical properties. Inorg. Chem. 2006; 45(21):8543–50.

[27] Fang B, Kim M, Kim JH, Yu J. Controllable synthesis of hierarchical nanostructured hollow core/mesopore shell carbon for electrochemical hydrogen storage. Langmuir 2008; 24(20):12068–72.

[28] Liu R, Lun N, Qi Y-X, Zhu H-L., Bai Y-J, Bi J-Q. Synthesis of hollow carbon sphere/ZnO@C composite as a light-weight microwave absorber. J. Phys. D: Appl. Phys. 2011; 44(26):265502.

[29] Bychanok D, Li S, Sanchez-Sanchez A, Gorokhov G, Kuzhir P, Ogrin FY, et al. Hollow carbon spheres in microwaves: Bio inspired absorbing coating Appl. Phys. Lett. 2016; 108:013701.

[30] Yu JS, Yoon SB, Lee YJ, Yoon KB. Fabrication of bimodal porous silicate with silicalite-1 core/mesoporous shell structures and synthesis of nonspherical carbon and silica nanocases with hollow core/mesoporous shell structures J. Phys. Chem. B 2005; 109(15):7040–5.

[31] Zhang L, Roy S, Chen Y, Chua EK, See KY, Hu X, et al. Mussel-inspired polydopamine coated hollow carbon microspheres, a novel versatile filler for fabrication of high performance syntactic foams. ACS Appl. Mater. Interfaces, 2014; 6(21):18644–52.

[32] Kim S, Shibata E, Sergiienko R, Nakamura, T. Purification and separation of carbon nanocapsules as a magnetic carrier for drug delivery systems. *Carbon* 2008; 46(12):1523–9.

[33] Guo, J. Zhang H, Geng H, Mi X, Ding G, Jiao Z. Efficient one-pot synthesis of peapod-like hollow carbon nanomaterials for utrahigh drug loading capacity. J. Colloid Interface Sci. 2015; 437:90–6.

[34] Fuertes AB, Sevilla M, Valdes-Solis T, Tartaj P. Synthetic route to nanocomposites made up of inorganic nanoparticles confined within a hollow mesoporous carbon shell. Chem. Mater. 2007; 19:5418–23.

[35] Valle-Vigón P, Sevilla M, Fuertes AB. Synthesis of uniform mesoporous carbon capsules by carbonization of organosilica nanospheres. Chem. Mater. 2010; 22:2526–33.

[36] Guo S-R, Gong J-Y, Jiang P, Wu M, Lu Y, Yu S-H. Biocompatible, luminescent Silver@Phenol formaldehyde resin core/shell nanospheres: Large-scale synthesis and application for in vivo bioimaging. Adv. Funct. Mater. 2008; 18(6):872–9.

[37] Fang Y, Guo S, Li D, Zhu C, Ren W, Dong S, et al. Easy synthesis and imaging applications of cross-linked green fluorescent hollow carbon nanoparticles. *ACS Nano* 2012, 6(1):400–9.

[38] Ghasemi H, Ni G, Marconnet AM, Loomis J, Yerci S, Miljkovic N, et al. Solar steam generation by heat localization. Nat. Commun. 2014; 5:4449.

[39] Taylor RA, Phelan PE, Otanicar TP, Walker CA, Nguyen M, Trimble S, et al. Applicability of nanofluids in high flux solar collectors. J. Renew. Sustain. Energy 2011; 3: 023104.

[40] Lenert A, Wang EN. Optimization of nanofluid volumetric receivers for solar thermal energy conversion. Sol. Energy 2012; 86:253–65.

[41] Nie Z, Bu L, Zheng M, Huang W. Experimental study of natural brine solar ponds in Tibet. Sol. Energy 2011; 85:1537–42.

[42] Yang M, Zhang M, Kunioda M, Yuge R, Ichihashi T, Iijima S, et al. Photothermal conversion of carbon nanohorns enhancing caprolactone polymerization. Carbon 2015; 83:15–20.

[43] Palomo Del Barrio E, Cadoret R, Daranlot J, Achchaq F. New sugar alcohols mixtures for long-term thermal energy storage applications at temperatures between 70°C and 100°C. Sol. Energy Mater. Sol. Cells 2016; 155:454–68.

[44] Ballweg T, von Daake H, Hanselmann D, Stephan D, Mandel K, Sextl G. Versatile triggered substance release systems via a highly flexible high throughput encapsulation technique. Appl. Mater. Today 2018; 11:231-7.

[45] Qi Y, Zhang M, Qi L, Qi Y. Mechanism for the formation and growth of carbonaceous spheres from sucrose by hydrothermal carbonization. RSC Adv. 2016; 6:20814–23.

[46] Sevilla M, Fuertes AB. Chemical and structural properties of carbonaceous products obtained by hydrothermal carbonization of saccharides. Chem. - A Eur. J. 2009; 15:4195–4203.

[47] Titirici M-M, White RJ, Falco C, Sevilla, M. Black perspectives for a green future: hydrothermal carbons for environment protection and energy storage. Energy Environ. Sci. 2012; 5:6796–6822.

[48] Braghiroli FL, Fierro V, Izquierdo MT, Parmentier J, Pizzi A, Celzard A. Kinetics of the hydrothermal treatment of tannin for producing carbonaceous microspheres. Bioresour. Technol. 2014; 151:271–7.

[49] Braghiroli FL, Fierro V, Izquierdo MT, Parmentier J, Pizzi A, Celzard A. Nitrogen-doped carbon materials produced from hydrothermally treated tannin. Carbon. 2012; 50 (15):5411–20.

[50] Marsh H, Warburton AP. Catalysis of graphitisation. J. Appl. Chem. 1970; 20:133–142.

[51] Extrand CW, Sung In Moon. Contact Angles on Spherical Surfaces, Langmuir 2008; 24(17): 9470-3.

[52] Celzard A, Fierro V, Amaral-Labat G, Szczurek A, Braghiroli F, Parmentier J, et al. Carbon gels derived from natural resources (Geles de carbón de origen natural). Boletín del Grupo Español del Carbón n°26/Decembre 2012; p. 2-7.

[53] Narasimman R, Prabhakaran K. Preparation of carbon foams by thermo-foaming of activated carbon powder dispersions in an aqueous sucrose resin. Carbon 2012; 50:5583–93.

[54] Braghiroli FL, Fierro V, Izquierdo MT, Parmentier J, Pizzi A, Delmotte L. High surface – Highly N-doped carbons from hydrothermally treated tannin. Ind. Crop. Prod. 2015; 66:282–90.

[55] Pizzi A. Monomers, Polymers and Composites from Renewable Resources, Elsevier, 2008:179–199.

[56] Inagaki M, Kang F. Materials Science and Engineering of Carbon: Fundamentals, Elsevier, 2014.

[57] Jana P, Palomo del Barrio E, Fierro V, Medjahdi G, Celzard A. Design of carbon foams for seasonal solar thermal energy storage. Carbon 2016; 109: 771-87.

[58] Swank WD, Valentin FI, Kawaji M, McEligot DM. Thermal Conductivity of G-348 Isostatic Graphite. Nucl. Technol. 2017; 199(1):103-9.

[59] Jana P, Fierro V, Celzard A. Sucrose-based carbon foams with enhanced thermal conductivity. Ind. Crops Prod. 2016; 89:498-506.

[60] Maire J, Mering J. Graphitisation of soft carbons. In: Walker PL, editor. Chemistry and Physics of Carbon. Vol 6, New York: Marcel Dekker; 1970, p. 125-89.

[61] Lespade P, Marchand A, Couzi M, Cruege F. Caractérisation de matériaux carbonés par microspectrométrie Raman. Carbon 1984; 22:375–85.

[62] Bernard S, Beyssac O, Benzerara K, Findling N, Tzvetkov G, Brown GE. XANES, Raman and XRD study of anthracene-based cokes and saccharose-based chars submitted to high-temperature pyrolysis Carbon 2010; 48(9):2506–16.

[63] Cançado LG, Jorio A, Pimenta MA. Measuring the absolute Raman cross section of nanographites as a function of laser energy and crystallite size. Phys. Rev. B 2007; 76(6):064304-1 – 7.

[64] Ferrari AC, Robertson J. Interpretation of Raman spectra of disordered and amorphous carbon, Phys. Rev. B 2000; 61(20):14095-107.

[65] Zeng Y, Wang K, Yao J, Wang H. Hollow carbon beads for significant water evaporation enhancement. Chem. Eng. Sci. 2014;116:704-9.

[66] Cengel YA. Heat Transfer: A Practical Approach, second ed., McGraw-Hill, New York, 2002.

[67] Gibson LJ, Ashby MF. Cellular Solids: Structure and Properties, second ed., Cambridge Solid State Press, Cambridge University Press, 1997.